J. Fluid Mech. (1980), *vol.* 101, *part* 3, *pp.* 493–544
Printed in Great Britain

Vortex pairing in a circular jet under controlled excitation. Part 2. Coherent structure dynamics

By A. K. M. F. HUSSAIN AND K. B. M. Q. ZAMAN
Department of Mechanical Engineering, University of Houston, Texas 77004

(Received 5 April 1979 and in revised form 20 February 1980)

The coherent structure dynamics in the near field of a circular jet has been experimentally explored by inducing 'stable' vortex pairing through controlled excitation (see Zaman & Hussain 1980) and applying phase-averaging techniques. Hot-wire measurements were made in a 7·62 cm air jet with laminar exit boundary layer at the Reynolds number $Re_D = 3{\cdot}2 \times 10^4$, excited at the Strouhal number $St_D = 0{\cdot}85$. At a particular phase during the pairing process, spatial distributions of the phase-average longitudinal and lateral velocity perturbations ($\langle u \rangle, \langle v \rangle$), vorticity, streamlines, the coherent and background Reynolds stresses and turbulence intensities have been educed. These data have been obtained for four different locations occupied by the vortices at the same phase (preceding, during, and following the pairing event), in the region $0 < x/D < 5$. Spatial distributions of these measures at four successive phases during the pairing process are also educed in an attempt to further understand the vortex-pairing dynamics. The flow physics is discussed on the basis of measurements over the physical extent of the vortical structures, phase-locked to specific phases of the pairing event and thus do not involve use of the Taylor hypothesis.

The computed pseudostream functions at particular phases are compared with the corresponding streamlines drawn by the method of isoclines. Transition of the vortices is examined on the basis of vorticity diffusion, the superimposed random fluctuation field intensities and Reynolds stress and phase-locked circumferential correlation measurements. The peak vorticity drops rapidly owing to transition and interaction of the vortices during pairing but, farther downstream, the decay can be attributed to destruction of the coherent vorticity by the background turbulence Reynolds stress, especially at the locations of the latter's 'saddle points'. Controlled excitation enhances the initial circumferential coherence of the vortical structures, but is ineffective in delaying turbulent breakdown near the end of the potential core; the breakdown appears to occur through evolution of the circumferential lobe structures. The coherent structure Reynolds stress is found to be much larger than the background turbulence Reynolds stress for $0 < x/D \lesssim 3$, but these two are comparable near the end of the jet potential core. The zone average of the coherent structure Reynolds stress over the cross-section of the merging vortex pair is much larger than that over a single vortical structure either before or after the completion of pairing. During the pairing process, such average correlations are found to be the largest at an early phase of the process while entrainment, turbulent breakdown as well as rapid diffusion of vorticity occur at a later phase. The regions of alternate positive and negative coherent Reynolds stresses associated with the structures and their interactions help explain 'negative production'.

0022-1120/80/4567-2550 $02.00

1. Background

The discovery of the quasi-deterministic structures in flows that otherwise would be characterized as fully turbulent (Brown & Roshko 1974; Winant & Browand 1974) have engendered widespread enthusiasm among researchers based upon the expectation that knowledge of the coherent structures may be crucial to the understanding and modelling of shear-flow turbulence.

The large-scale coherent structures in the near-fields of three circular air jets were experimentally investigated by organizing these structures through controlled acoustic excitation, induced in the jet via cavity resonance produced by a loudspeaker attached to the settling chamber. The response of the jet to excitation as a function of the Strouhal number and the Reynolds number was studied for both initially laminar and tripped boundary layers by Zaman & Hussain (1980; hereinafter referred to as I). It was shown that vortex pairing in the jet can be stabilized or suppressed depending on the Strouhal number. The present paper discusses the detailed field measurements associated with the near-field coherent structures under the conditions of stable vortex pairing.

There have been two alternative approaches to studying the large-scale coherent structures. One is to detect the naturally occurring structures through some form of conditional sampling and to obtain an ensemble average to deduce their characteristics (Kovasznay, Kibens & Blackwelder 1970; Lau & Fisher 1975; Browand & Wiedman 1976; Bruun 1977; Yule 1978). While this approach is more relevant to the practical flow, it suffers from some constraints. First, since the data acquisition and analysis must follow detection, signals should either be recorded or, when analysing real time, the signal must be delayed without distortion. Secondly, because of the dispersion in shape, size, orientation, strength, and convection velocity, successive realizations do not capture the same cross-section of the structure; choice of a multiple-sensor probe may significantly alleviate this problem. Thirdly, the eduction is dependent on a subjectively determined detection scheme; this introduces not only a judgement factor, but also the possibility that different detection schemes may produce different descriptions of the same structure. The educed structure and its convection velocity in a mixing layer depend on whether the positive or negative spikes in the u signal are used for the detection (Bruun 1977). The structure interactions like pairing or tearing, which occur randomly, further complicate eduction and interpretation of the coherent structure dynamics. Fourthly, such eduction of the naturally occurring structures would be prohibitively time-consuming.

The alternative approach is to induce a periodic perturbation in the flow and use the period as a clock for detection of the structure. The ensemble average at a particular phase at a station gives the phase average of the structure. Even though the question arises as to whether the induced structure truly resembles the naturally occurring structure or not, this approach is highly attractive and has been followed rather successfully in a number of investigations (Hussain & Reynolds 1970; Crow & Champagne 1971; Wygnanski, Sokolov & Friedman 1976; Zilberman, Wygnanski & Kaplan 1977; Cantwell, Coles & Dimotakis 1978; Cantwell & Coles 1978, private communication; Hussain & Thompson 1980; Sokolov *et al.* 1980). This approach has been the basis of the present investigation.

Application of the phase-averaging technique to study the vortex-pairing

phenomenon was rendered possible by our earlier success in inducing 'stable' vortex pairing (Hussain & Zaman 1975). As discussed in I, even under excitation, the pairing phenomenon can occur at random in space and time as is the case in an unperturbed flow. Only under specific excitation conditions, 'stable' vortex pairing can be induced when, at a given spatial location, the same phase of the pairing event can be captured at periodic intervals, except for some unavoidable jitter. Thus, an ensemble average of the data at a particular phase will reveal the dynamics of the event at that phase. For a typical 'stable' vortex pairing in the 'jet-column mode' (see I), the spatial distributions of phase-average properties at different phases of the pairing event as well as in regions preceding and following the pairing location are discussed in the following. These data reveal heretofore unreported aspects of the coherent vortical structures and pairing in the axisymmetric mixing layer.

For descriptions of the flow facility and instrumentation, documentation of the exit and jet flow characteristics in the absence of the perturbation, and further details, see I.

2. Procedures

2.1. *Phase average and consequences*

The eduction of the coherent structure signature as well as interpretation of the data require introduction of the concept of phase average (Hussain & Reynolds 1970; Hussain 1977) and its consequences like coherent Reynolds stress *vs.* background Reynolds stress. One can regard any instantaneous flow variable f to consist of the contributions from the global (time) mean field $\bar{f}$, the (periodic) coherent field $\tilde{f}$ and the background turbulent (fluctuation) field f', i.e.

$$f(\mathbf{x},t) = \bar{f}(\mathbf{x}) + \tilde{f}(\mathbf{x},t) + f'(\mathbf{x},t), \tag{2.1}$$

where

$$\bar{f} = \lim_{\bar{T}\to\infty} \frac{1}{\bar{T}} \int_0^{\bar{T}} f(t)\,dt. \tag{2.2a}$$

If we use angle brackets to denote the phase average at a particular time t in the period T of the periodic perturbation, then

$$\langle f(\mathbf{x},t)\rangle = \lim_{N\to\infty} \frac{1}{N} \sum_{n=1}^{N} f(\mathbf{x}, t+nT), \tag{2.2b}$$

so that $\langle f\rangle = \bar{f}+\tilde{f}$. The difference between the instantaneous signal and the phase average represents the background random fluctuation, and the difference between the phase average and the time average denotes the (periodic) coherent component. Thus, knowing the period of the induced perturbation, the mean, coherent and random components of the signal can be extracted from the instantaneous total signal.

A few consequences of the time- and phase-averaging schemes follow:

$$\langle f'\rangle = \bar{f}' = \tilde{\bar{f}} = 0; \quad \langle \tilde{f}g\rangle = \tilde{f}\langle g\rangle; \quad \langle \bar{f}g\rangle = \bar{f}\langle g\rangle; \quad \langle \tilde{f}g'\rangle = \overline{\tilde{f}g'} = 0. \tag{2.3}$$

The last two equations state that, on average, periodic and random components are uncorrelated.

Substitution of the decomposition (2.1) into the incompressible continuity and momentum balance equations gives

$$\frac{\partial \bar{u}_i}{\partial x_i} = \frac{\partial \tilde{u}_i}{\partial x_i} = \frac{\partial u_i'}{\partial x_i} = 0; \tag{2.4}$$

$$\frac{\bar{D}\bar{u}_i}{Dt} = -\frac{1}{\rho}\frac{\partial \bar{p}}{\partial x_i} + \nu \frac{\partial^2 \bar{u}_i}{\partial x_j \partial x_j} + \frac{\partial}{\partial x_j}(-\overline{\tilde{u}_i \tilde{u}_j} - \overline{u_i' u_j'}), \tag{2.5a}$$

$$\frac{\bar{D}\tilde{u}_i}{Dt} = -\frac{1}{\rho}\frac{\partial \tilde{p}}{\partial x_i} + \nu \frac{\partial^2 \tilde{u}_i}{\partial x_j \partial x_j} + \frac{\partial}{\partial x_j}(-\bar{u}_i \tilde{u}_j) - \frac{\partial}{\partial x_j}(\langle \tilde{u}_i \tilde{u}_j \rangle - \overline{\tilde{u}_i \tilde{u}_j}) - \frac{\partial}{\partial x_j}(\langle u_i' u_j' \rangle - \overline{u_i' u_j'}), \tag{2.5b}$$

where $\bar{D}/Dt = \partial/\partial t + \bar{u}_j \partial/\partial x_j$ is the material derivative in the time-mean flow field. Thus, the time-mean Reynolds stress consists of two parts, one contributed by the (periodic) coherent part and one by the (random) background turbulence. Since only the coherent part of the motion is assumed periodic, it is reasonable to call $\langle \tilde{u}_i \tilde{u}_j \rangle$ the phase average of the coherent structure Reynolds stress and $\langle u_i' u_j' \rangle$ the phase-average background Reynolds stress. For additional equations and detailed discussion of the flow physics, see Reynolds & Hussain (1972) and Hussain (1977).

The decomposition (2.1) assumes the coherent structure to be a perturbation superimposed on the mean flow field. However, at the location of a structure, the flow is essentially due to the structure. Consequently, it is probably more appropriate to view the flow field from the coherent structure field. (For the continuity, momentum and energy equations for the coherent and background turbulent motions and detailed discussion of the flow physics viewed this way, see Hussain 1977.)

For convenience, let us use $\tilde{f}$ to denote the instantaneous variable f, f_p its periodic part, f_r its random part and f' the r.m.s. values of f. Thus,

$$\tilde{u}(\mathbf{x}, t) = U(\mathbf{x}) + u_p(\mathbf{x}, t) + u_r(\mathbf{x}, t); \quad \tilde{v}(\mathbf{x}, t) = V(\mathbf{x}) + v_p(\mathbf{x}, t) + v_r(\mathbf{x}, t).$$

Also, $\langle \tilde{u} \rangle = U + u_p$ will be denoted by $\langle u \rangle$ and $\langle \tilde{v} \rangle = V + v_p$ by $\langle v \rangle$. Note that

$$\langle \{\tilde{u} - U\}\{\tilde{v} - V\} \rangle \equiv \langle uv \rangle = \langle u_p u_p \rangle + \langle u_r v_r \rangle \tag{2.6}$$

since $\langle u_r v_p \rangle$ and $\langle u_p v_r \rangle$ are zero according to the last relation in (2.3). Thus, $\langle u_p v_p \rangle$ represents the phase average of the Reynolds stress due to the large-scale coherent motions, and $\langle u_r v_r \rangle$ that due to the background turbulence. Note that (2.6) does not include the total momentum transport at any phase since $U v_p + u_p V$ also represent the phase-average transport of mean momenta by the coherent structure (equation (2.5*b*)). Note also that the last two relations in (2.3) do not suggest that the coherent field and the background turbulent field are unrelated. The quantity $\langle u_r v_r \rangle$ represents the effect of the coherent structure on the background turbulence field. However, this effect of the coherent structure is indirect in the sense that the periodic modulation does not directly contribute to $\langle u_p \rangle$, $\langle v_p \rangle$, $\langle u_p v_p \rangle$, etc. since the time scale of the coherent structure is much larger than that of the background turbulent fluctuations.

2.2. *Data acquisition and reduction*

Data presented in this paper cover spatial distributions of U, V, $\langle u \rangle$, $\langle v \rangle$, $\langle u_p v_p \rangle$, $\langle u_r v_r \rangle$ as well as $\langle u_r^2 \rangle^{\frac{1}{2}}$, $\langle v_r^2 \rangle^{\frac{1}{2}}$ (the phase-average intensities of $u_r(t)$ and $v_r(t)$); the last two being defined as

$$\langle f_r^2 \rangle^{\frac{1}{2}} = \left[\lim_{N \to \infty} \frac{1}{N} \sum_{n=1}^{N} f_r^2(\mathbf{x}, t + nT) \right]^{\frac{1}{2}}. \tag{2.7}$$

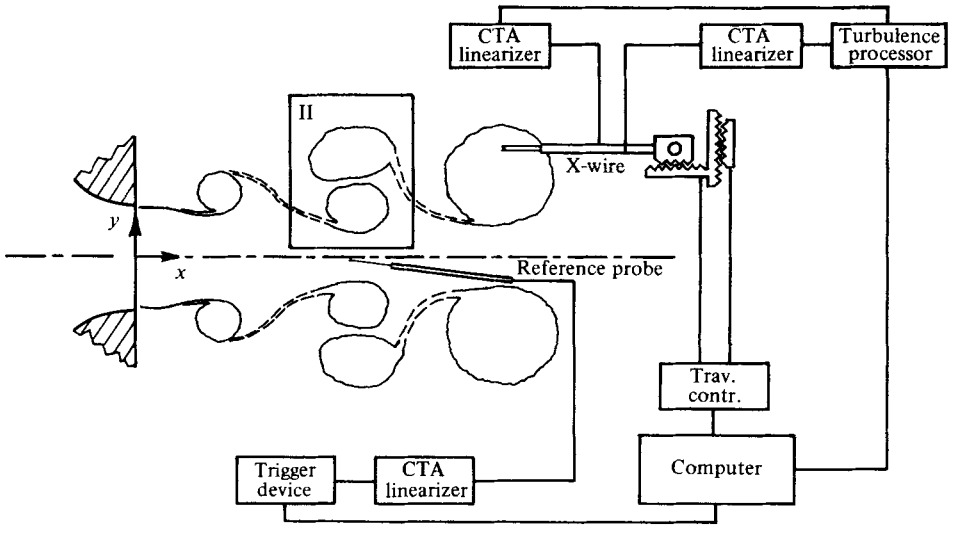

FIGURE 1. Schematic diagram of the jet coherent structure and instrumentation.

Phase-average measurements were carried out at a large number of spatial points in a selected 'region' on the radial (x, y) plane, thus providing a spatial distribution of the variable in the region at a particular phase. The phase was chosen to capture a selected phase of the vortex-pairing event. A schematic diagram of the flow situation and the relative vortex locations at the chosen phase are shown in figure 1. Also shown are the reference (single-wire) and the measurement (X-wire) probes, instrumentation and co-ordinates (see also figure 1 in I).

The phase-average data at any grid location were acquired on-line with the laboratory minicomputer system (HP 2100S). The signals $\tilde{u}(t)$, $\tilde{v}(t)$ and $\widetilde{uv}(t)$ were sampled by the computer at desired phases. These signals were obtained from a turbulence processor (DISA Model 52B25) which decomposes the two a.c.-coupled signals from linearized DISA constant-temperature anemometers operating the X-wire. Averages over a large number of samples (typically 1920 samples) gave the different phase-average quantities as functions of (x, y) in each flow 'region' (see § 2.3).

(*a*) *Triggering procedures.* In the presence of stable vortex pairing, the centre-line velocity signal in the potential core in the region of vortex pairing is periodic at half of the excitation frequency f_p (see I). The output of the reference probe located on the jet centre-line at $x/D \approx 1{\cdot}5$, band-pass filtered at the pairing frequency, provided the reference signal which activated a triggering device. The output of the triggering device was a pulsed output signal (the triggering signal) of frequency $\frac{1}{2}f_p = 35$ Hz. When the reference signal exceeded a set threshold level with positive slope, the output from the triggering device jumped to a high level and remained there for an adjustable time before dropping to zero. The $\tilde{v}(t)$ signal from the X-wire showed zero-crossing with a large positive slope at the instant when the vortex centre was at the X-wire. By choosing the 'dwell' time, the time delay τ between the instant for trigger signal drop and the instant for vortex centre passage could be changed and thus a desired phase for data sampling could be chosen. At the instants the triggering signal dropped from the high level to zero, the analog-to-digital converter was activated to sample the

appropriate signals. At each trigger, the three signals were sequentially sampled at 25 kHz and thus the three data could be regarded as simultaneous.

(*b*) *Vorticity computation and other considerations.* A self-convergent criterion was used for acquisition of the phase-locked data to avoid prohibitively long experiment times while simultaneously limiting the data scatter within acceptable bounds. For the contour plots to be discussed later, a data-smoothing scheme was incorporated using a dynamic least-squares fit technique – the same scheme was also used to compute the z component of the phase-average vorticity $\zeta_z(x, y; t) \equiv \Omega$ from the $\langle u\rangle(x, y)$ and $\langle v\rangle(x, y)$ arrays. The uncertainty bounds in the $\langle u\rangle/U_e$ and $\langle v\rangle/U_e$ data are estimated to be about 5 %.

For further details of the data acquisition, triggering device, error estimates and data-smoothing techniques, see Zaman (1978).

2.3. *Choice of the measurement regions*

Even though the controlled excitation organizes and stabilizes the vortex-pairing phenomenon, quantitative measurements of the near-field coherent structure are not free from ambiguity. The comparatively straightforward approach of using a stationary probe and educing the coherent structure signature from the velocity signals by ensemble averaging has been followed by investigators of coherent structures (Coles & Barker 1975; Wygnanski *et al.* 1976; Zilberman *et al.* 1977; Browand & Wiedman 1976; Yule 1978), but this approach suffers from the limitation that data associated with different spatial points of the structure are captured at different times. To obtain a physical description of the structure in the (x, y) plane from the data in (t, y), one must invoke the Taylor hypothesis whose applicability to turbulent shear flows in general and to the large-scale coherent structures in particular is questionable. In the latter case, at least two major limitations of the Taylor hypothesis, namely, low shear and small fluctuation intensity, are violated (Lin 1953). Consider that $u'(x', t')$ is the streamwise velocity when viewed from a reference frame (x', t') convected downstream with a velocity U_c, then

$$x' = x - U_c t; \quad u'(x', t') = u(x, t) - U_c. \tag{2.8a}$$

Since $\partial t'/\partial t = 1$,

$$\left.\frac{\partial u(x,t)}{\partial t}\right|_x = \frac{\partial u'}{\partial x'}\frac{\partial x'}{\partial t} + \frac{\partial u'}{\partial t'}. \tag{2.8b}$$

Thus, if an observer moving with the convected frame sees insignificant change of the coherent structure, which is a reasonable assumption for short time intervals, the second term on the right-hand side of (2.8*b*) is negligible, and

$$\frac{\partial u'}{\partial x'} = -\frac{1}{U_c}\frac{\partial u}{\partial t}. \tag{2.8c}$$

Clearly, even if U_c is used for the transformation of temporal gradients to spatial gradients, the variation of the convection velocity U_c in time and space, together with the continuous distortion and rotation of the structure, would frustrate any effort to understand clearly the coherent structure dynamics. It was thus felt that a true spatial distribution of the structure-induced motion was necessary. Since by controlled excitation the structure could be induced to occur periodically at specified locations,

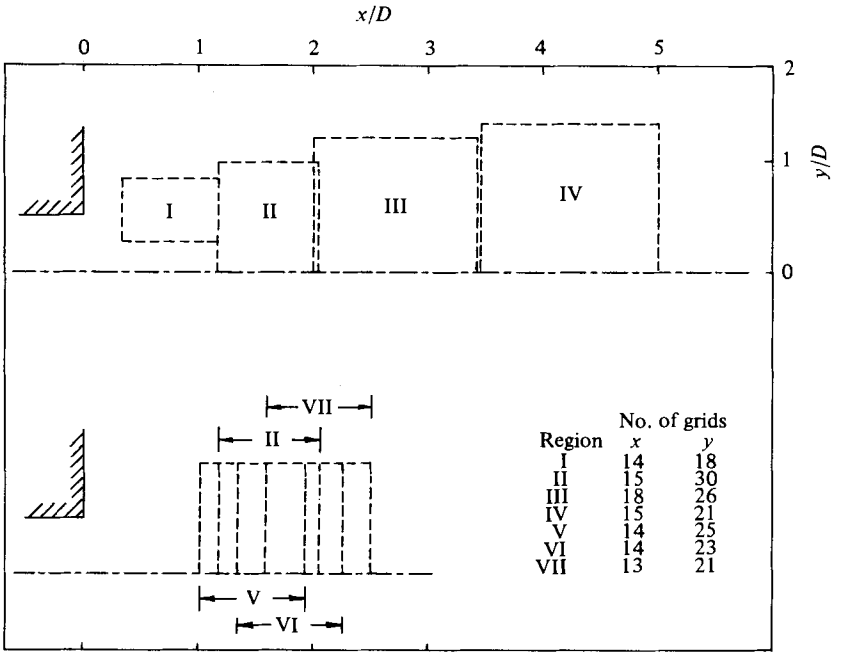

FIGURE 2. The measurement 'regions' I–VII. The number of spatial grids in (x, y) in each region is indicated.

it was possible to obtain the phase-average property at a point using a single probe. By changing the probe location and repeating phase-average measurements locked to the same phase of the event, the actual spatial distribution of a flow property in the (x, y) plane at one instant could be directly obtained without involving the Taylor hypothesis. Thus this alternative, albeit far more arduous, route of obtaining the spatial details of the larger-scale coherent structure was chosen.

Such spatial measurements could be taken at different times (i.e. phases) during the evolution of the coherent structure. It was decided to carry out the measurements within the axisymmetric mixing layer up to the end of the potential core at one particular phase of the excitation. Within this length, the structure would typically be captured at three to four locations at any phase of the excitation. Deciding on the phase for flow documentation was clearly arbitrary.

The phase chosen was such that the two pairing vortex rings are in the middle of their pairing process, more specifically, in the same diametral plane. This choice, though arbitrary, was partly motivated by the fact that at this phase the two pairing vortices were in their most intense relative motion (see I) and by the observation based on flow-visualization experiments that the faster-moving inner vortex undergoes an explosive transition shortly after passing through this phase. For this particular phase, the flow field was divided into four spatial regions (I, II, III and IV) as shown in figure 2. Flow-visualization experiments showed that the two merging vortices underwent pairing in region II, while region III contained the combined vortex following the merger, and region I contained a type-2 vortex near the end of its roll-up (see I). Although flow-visualization revealed no clear vortical structure in region IV,

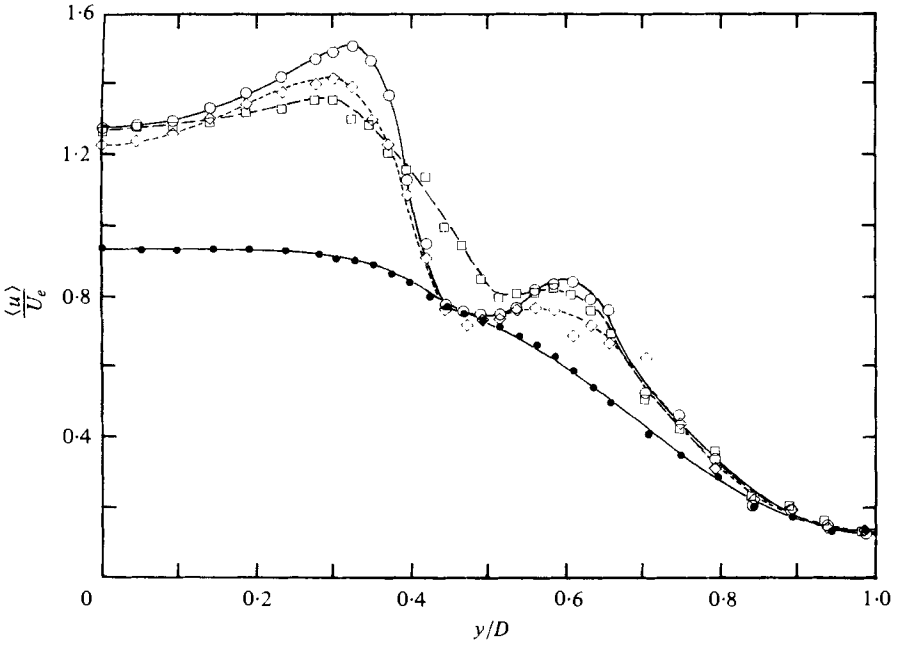

FIGURE 3. Phase-average longitudinal velocity profiles at: ◇, x = 11·11 cm; ○, x = 11·75 cm; □, x = 12·38 cm. ●, mean velocity profile at x = 11·75 cm.

measurements were carried out there in order to see if the phase-averaging technique could sift out the (probably hidden) underlying large-scale structure. The spatial region for measurements in three additional phases of the pairing process, encompassing the two pairing vortices only, are also shown in figure 2. Identified as regions V, VI and VII, these three are small variations of the region II. Thus regions V, II, VI and VII (characterized as phases 1, 2, 3, and 4, respectively) capture the details of the pairing event at close time intervals as the event progresses.

The spatial grid spacing for the measurement locations were chosen after preliminary investigations which showed that the measured vorticity at a particular location increased with decreasing grid size until a size was reached when further decreases did not noticeably alter it any more. The grid size was judiciously varied both in x and in y, with larger spacing on the periphery but finer spacings in the vortex core. The numbers of spatial grids used in each region are tabulated in the legend of figure 2.

3. Results and discussion

3.1. *Phase-average velocity distributions*

The phase-average profiles $\langle u \rangle (y)$ are shown in figure 3 for three x stations within the region II, at x = 11·11, 11·75 and 12·38 cm. The centres of the two pairing vortices are located at x = 11·75 cm in the 'radial configuration'; thus the stations x = 11·11 and 12·38 cm represent the trailing and the leading ends, respectively, of the vortex pair. Also shown in figure 3 is $U(y)$ for x = 11·75 cm. The $\langle u \rangle$ profiles can be qualitatively explained by considering the induced velocity fields of the two vortices at the phase

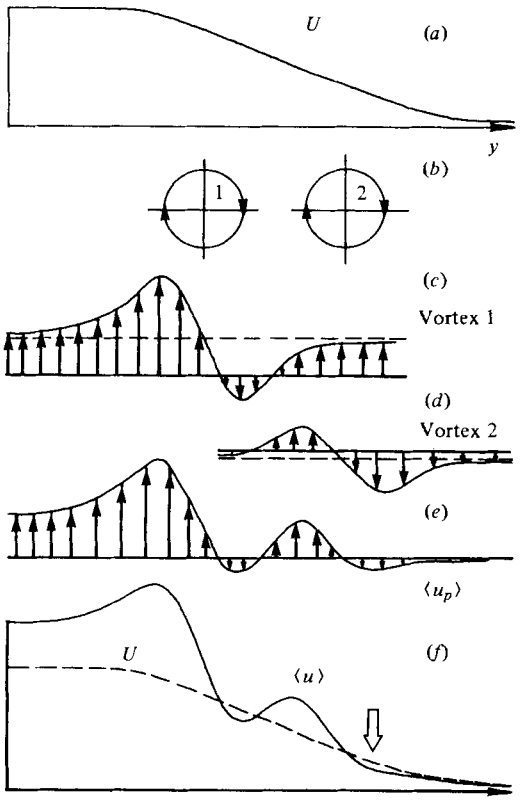

FIGURE 4. Explanation for induced longitudinal velocities due to the vortices.

under study, drawn schematically in figure 4. The mean velocity profile and the vortex pair locations are realistically sketched in (*a*) and (*b*) for the radial configuration of the two vortices. Vortex 1 moves much faster than vortex 2; the latter is also weaker than the former. The velocity fields of vortices 1 and 2 are sketched in (*c*) and (*d*) respectively, each with a bias velocity equal to the difference between the convection velocity of the vortex and the local mean velocity at its y location. Note that at this phase vortex 1 moves faster than the local mean velocity while vortex 2 moves slower than the local mean velocity (see I). Consequently, the combined velocity distribution due to the vortex pair will be as shown in figure 4(*e*). When this is superimposed on the mean velocity profile (figure 4*a*), the resulting velocity distribution (figure 4*f*) is not unlike the measured distribution in figure 3. The above qualitative explanation is for a plane configuration; if the axisymmetric configuration is taken into consideration, the theoretical model profiles will agree better with the data.

Note that the two other profiles $\langle u \rangle$ (y) in figure 3 also show dual, but weaker, humps so that the influence of the vortex pair is also fairly strongly felt at these two locations towards the front and rear ends of the vortex. But farther away on either side (in x) of each vortex, $\langle u \rangle$ would have contributions opposite to those shown in figure 4(*e*); for example see figure 7. The slight dip in the time-mean profile $U(y)$ in figure 3 can be attributed to the combined effects of the radial separation of the alternate vortices at this x location, as well as to the hot-wire response to large-amplitude fluctuations.

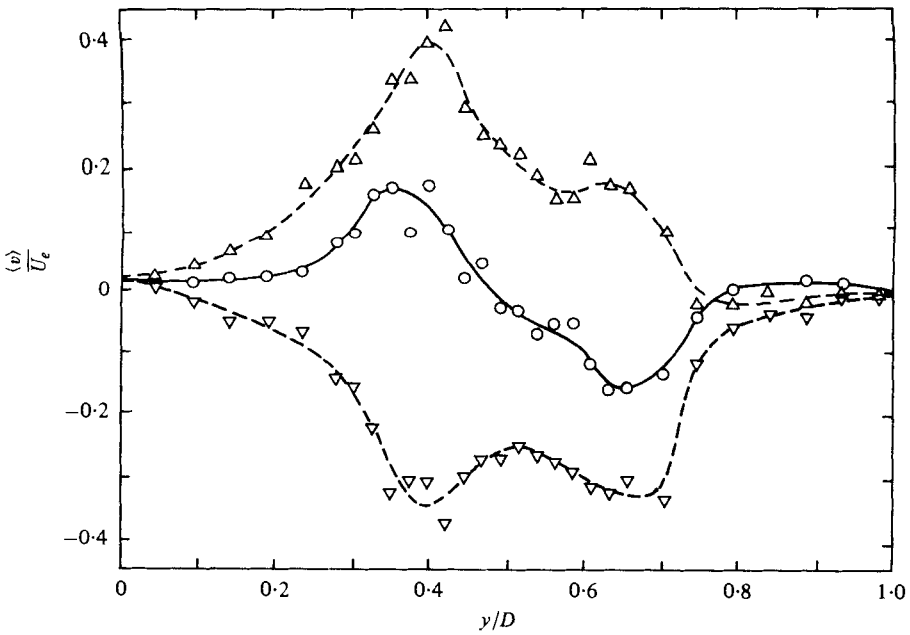

FIGURE 5. Phase-average transverse velocity profiles at: ▽, x = 11·11 cm; ○, x = 11·75 cm; △ x = 12·38 cm.

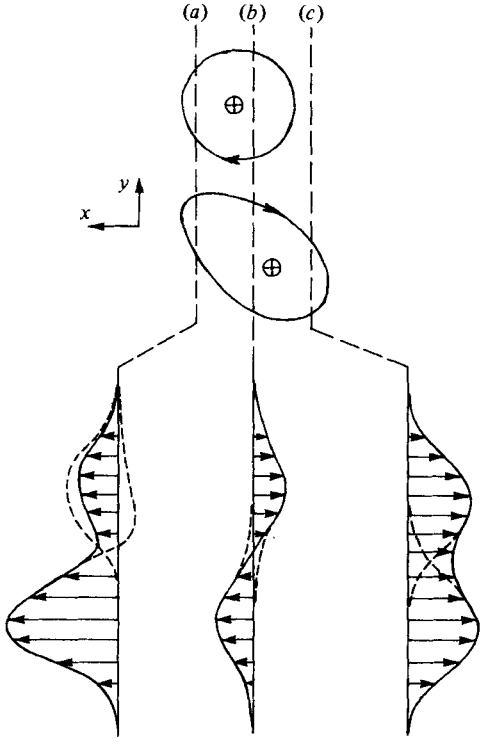

FIGURE 6. Explanation for induced transverse velocity profiles due to the vortices.

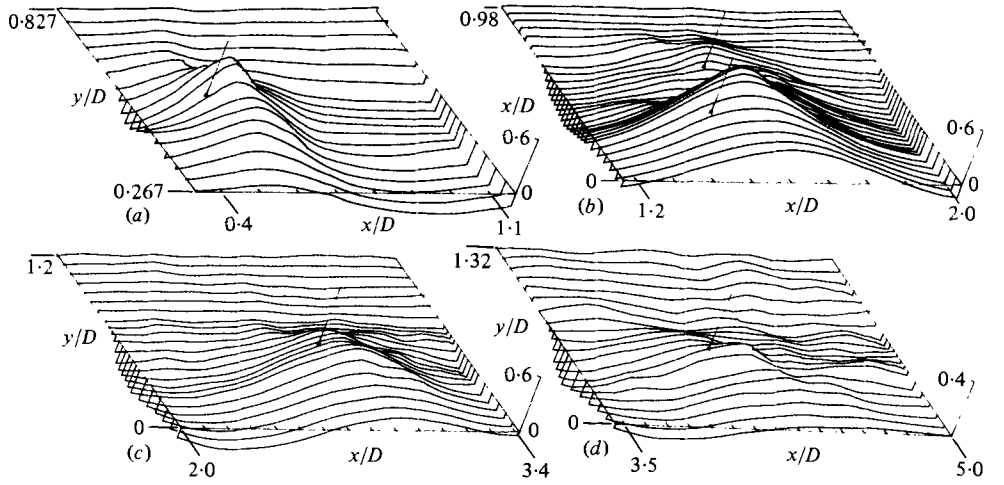

FIGURE 7. $\langle u_p \rangle / U_e$ distributions over the measurement regions: (*a*) region I; (*b*) region II; (*c*) region III; (*d*) region IV.

The measured phase-average $\langle v \rangle (y)$ profiles for the same three x stations of figure 3 are shown in figure 5. If the centres of the vortices were situated exactly on a radial line (i.e. at the same x) and the vortices were symmetric in x, the values of $\langle v \rangle$ everywhere on that radial line would be expected to be the same as the V value (i.e. almost zero). This condition is nearly met at $x = 11{\cdot}75$ cm, but $\langle v \rangle (y)$ here shows undulations because the centres of the two vortices are displaced slightly (in x) and the front and rear ends of the vortices are not symmetric about their centres (see later). As done in figure 4 for $\langle u \rangle (y)$ profiles, realistic transverse velocity profiles associated with the vortex pair sketched in figure 6 reasonably explain the $\langle v \rangle (y)$ variations of figure 5.

The phase-average $\langle u_p \rangle$ distributions in the (x, y) plane for regions I–IV are shown as relief maps in figures 7(*a*)–(*d*). The corresponding $\langle v_p \rangle$ maps are presented in figures 8(*a*)–(*d*). The centres of the vortices as determined from the vorticity contours (see later) are shown by the vertical lines with a cross-sign in the base plane. Curves at larger y stations crossing those at smaller y are not shown for visual clarity.

Note that even though the instantaneous signals contain large-amplitude random velocity fluctuations, the phase-averaging technique sifts out the coherent structure signatures. The region I represents essentially the conclusion stage of the vortex roll-up process, as seen in the flow visualization pictures (figure 9*a*). The corresponding streaklines of the rolled-up vortex are schematically shown in figure 9(*b*) (see plate 1). Consider the induced velocities along the dotted lines A and B as shown in the figure. Clearly, the induced streamwise velocity along the line B, which is on the inner i.e. the core side of the jet, will be maximum at an x station corresponding to the vortex centre. Thus the $\langle u_p \rangle (x)$ variation along B should be as shown qualitatively in the profile at the bottom of figure 9(*b*). Similarly, along A, the induced velocity $\langle u_p \rangle (x)$ should be negative like the profile shown qualitatively at the top of figure 9(*b*). Such variations of $\langle u_p \rangle (x)$ can be observed in figure 7(*a*). However, the profiles with the negative dips, radially outside the vortex centre, are weaker, as to be expected because

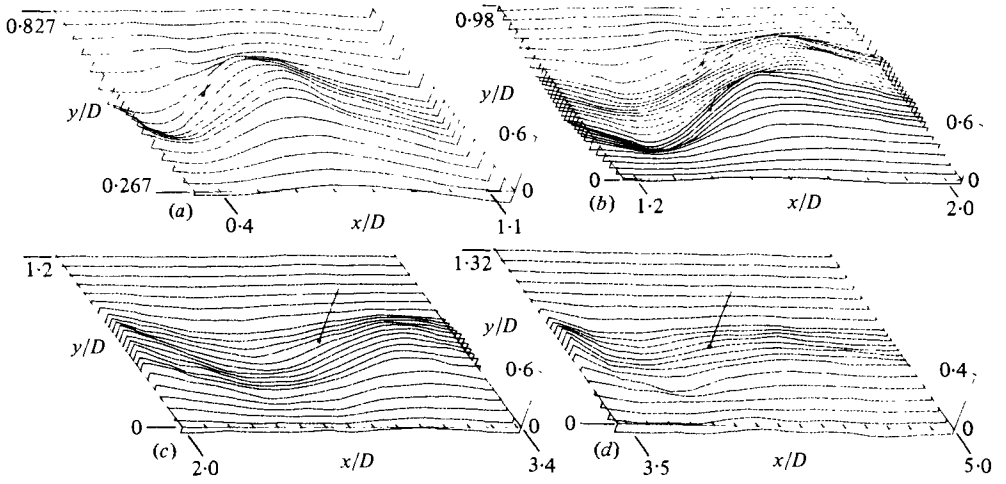

FIGURE 8. $\langle v_p \rangle / U_e$ distributions over the measurement regions I–IV: (*a*) region I; (*b*) region II; (*c*) region III; (*d*) region IV.

of the axisymmetric flow configuration. For example, compare the data represented by the 8th and 14th traces along increasing y in figure 7 (*a*) with the lower and upper profiles in figure 9 (*b*), respectively. In a similar manner, the measured distributions of $\langle v \rangle (x)$ can be explained satisfactorily.

In region I (containing a single rolled-up vortical structure), while the $\langle u_p \rangle$ profiles are approximately symmetric in x around the vortex centre, the $\langle v_p \rangle$ profiles appear antisymmetric, thus indicating small net contribution of the coherent structure to the time-average Reynolds stress. Similar characteristic distributions of $\langle u_p \rangle$ and $\langle v_p \rangle$ are also observed for regions III and IV, both of which contain single vortical structures (after the completion of pairing). For region II (and also for regions V, VI and VII for which these plots are not shown), on the other hand, the variations are complicated; especially in transverse regions between the two vortices (see figures 7*b* and 8*b*).

The phase-average total correlation $\langle uv \rangle (= \langle u_p v_p \rangle + \langle u_r v_r \rangle)$ profiles (in x) are shown only for regions II and III in figure 10 (*a*) and (*b*), respectively. Comparison of figure 10 (*a*) with figure 8 (*b*), for example, show that the asymmetry properties of $\langle v_p \rangle (x)$ profiles are carried onto $\langle uv \rangle (x)$ profiles. In general, however, as can be seen in figure 10 (*a*), the correlation value is positive over most of x at transverse locations that fall between the two pairing vortices.

3.2. *The vorticity contours*

The contours of constant phase average vorticity Ω, non-dimensionalized by f_p, in each of the seven measurement regions are shown in figures 11 (*a*)–(*g*). The roll-up of vortex 2 (one which decelerates during pairing, see I) can be seen in figure 11 (*a*) while the pairing process is captured for successive phases (1–4) in figures 11 (*e*), (*b*), (*f*) and (*g*), respectively. For these latter four cases, the delay time τ, taking the second (i.e. phase 2) as the reference phase, is shown in the legend. The 'dip' on the low-speed side

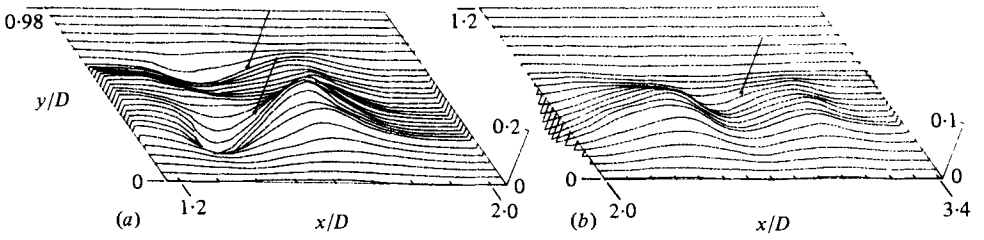

FIGURE 10. The $\langle uv\rangle/U_e^2$ distributions: (*a*) region II; (*b*) region III.

of the vorticity contours will be explained later. The phase-average constant vorticity contours, except for the low-speed side distortions, bear excellent resemblance to the smoke pictures discussed in I.

The roll-up process shifts the peak vorticity fluid towards the low-speed region, and the peak vorticity in the rolled-up vortex centre is much higher than that in the braid connecting it to the lip. More interesting is the fact that the 'braid' connecting the vortices in region I and II contains much lower vorticity (discussed later). It is clear that the vorticity from the initial boundary layer before separation is mostly accumulated in the cores of the rolled-up vortex rings; the ratio of the core peak vorticity in region I to the maximum mean vorticity in the initial boundary layer (which was measured 0·25 cm upstream from the nozzle exit and found consistent with the Blasius profile value) was about 0·60.

The choice of phases 2 and 3 of vortex pairing was motivated by the flow-visualization experiments, which showed a sudden diffusion of the smoke traces soon after the vortex 1 passed through the radial configuration. The other two phases (1 and 4) were chosen to determine if an earlier or a later phase in the pairing process has significantly different dynamical importance. The inclination of the line connecting the centres of the two merging vortices with the jet axis (see I) in phases 1 and 4 are slightly different (35° and 38°, respectively), although they were intended to be the same. This is so because there is no *a priori* method of accurately determining the time delay (i.e. phase) that will result after phase averaging.

The individual identities of the two pairing vortices are lost in region III as shown in figure 11(*c*). The two paired vortices may still retain some semblance of separate structures, but their small scales and the jitter from one realization to the next would not allow this remnant structure to be detected. Smoke traces in the visualization experiments also appear diffuse at this location, indicating somewhat uniform spread of turbulence throughout the entire core of the merged structure. This observation is also supported by the fact that the peak vorticity in this region is less than that of either of the two pairing vortices (figures 11*b*, *e*, *f*, *g*).

Circulation (Γ) measured by line integration of the phase-average velocities around a rectangle just enclosing the $\Omega/f_p = 1{\cdot}0$ contour was found to remain constant from region II to region III; this value of $\Gamma/U_e D$ was found to be approximately 1·0 for both the regions. The areas enclosed by the $\Omega/f_p = 1{\cdot}0$ contours in regions II and III were not significantly different: approximately 20 and 23 cm^2, respectively. Thus the average vorticity ($= \Gamma/\text{area}$) in regions II and III did not change appreciably; the sharp peaks in vorticity in region II (figure 11*b*) crumbled to a much lower plateau in region III (figure 11*c*). This rapid diffusion of vorticity within the core is believed to

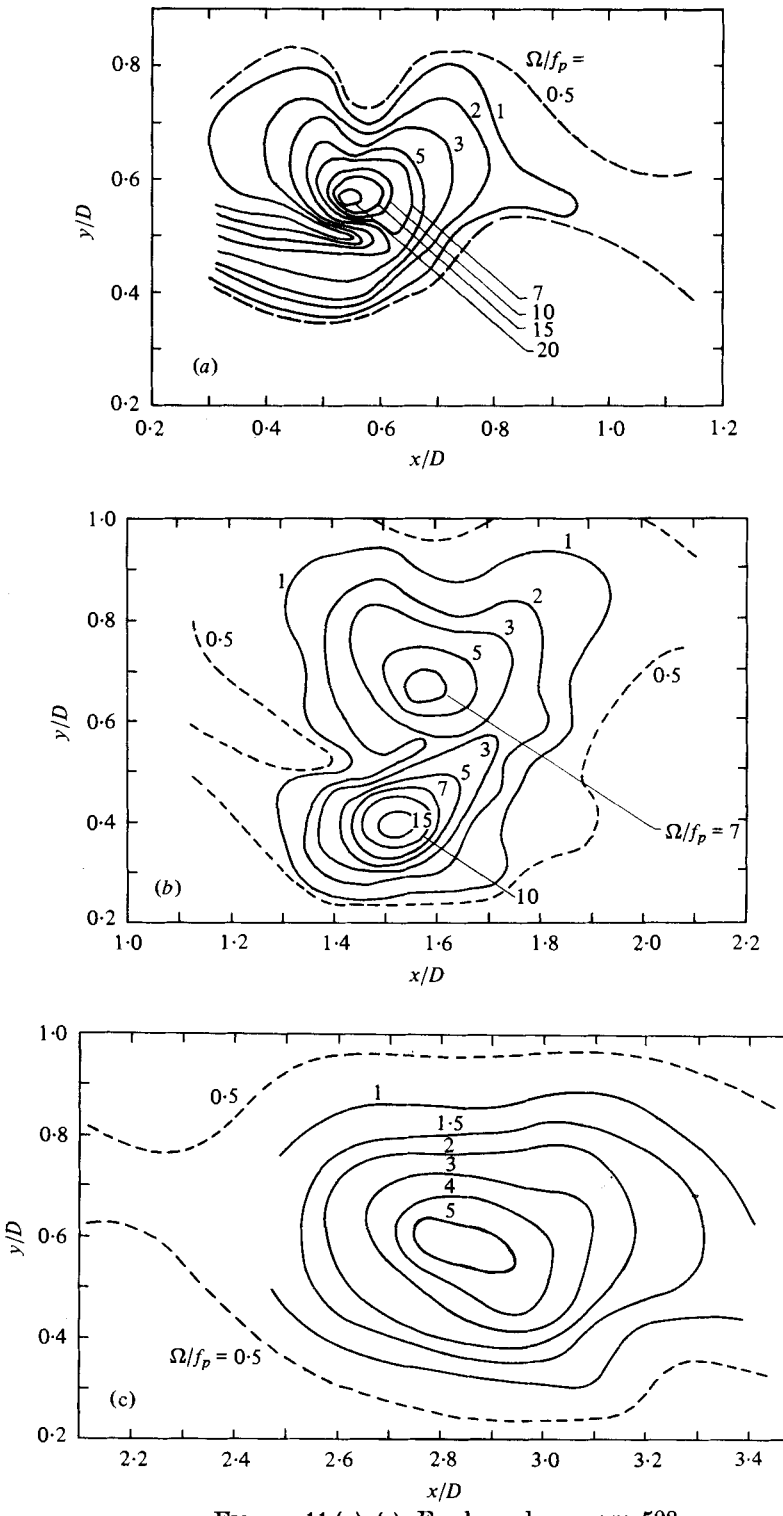

FIGURE 11 (*a*)–(*c*). For legend see page 508.

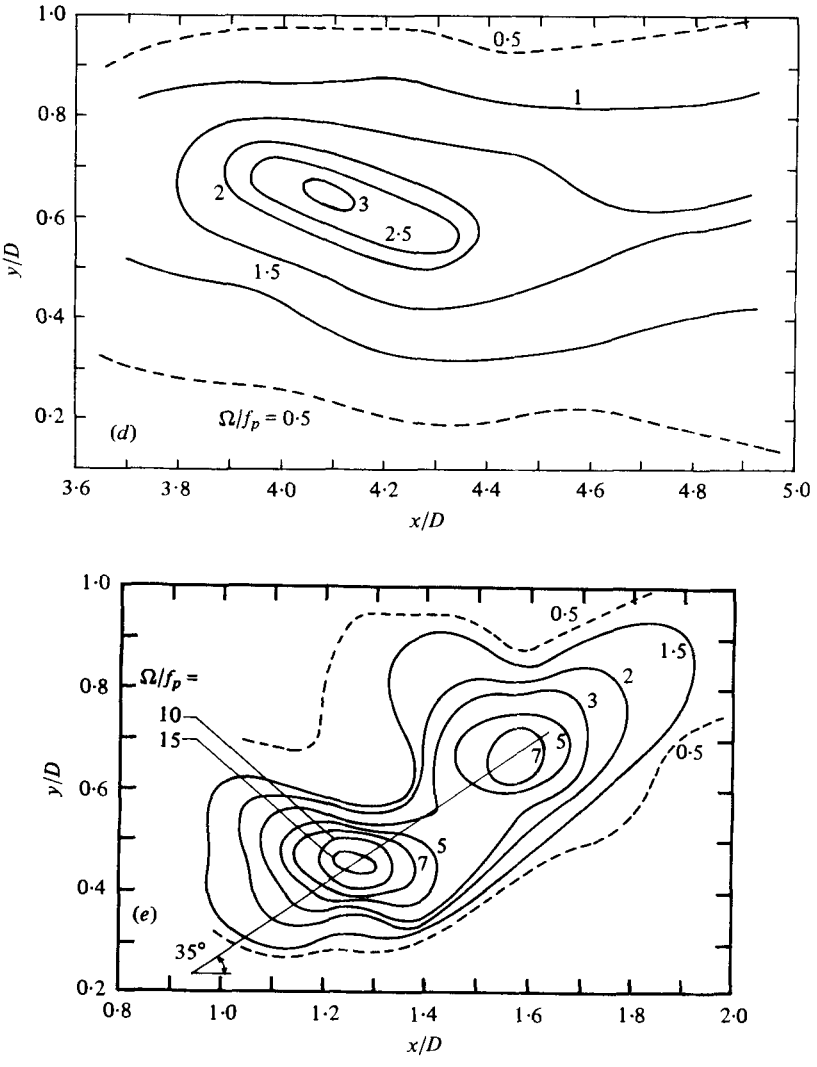

FIGURE 11 (*d*, *e*). For legend see page 508.

be due to the intense interaction of the two vortices, the associated entrainment, as well as to transition ensuing shortly after phase 2 in the pairing process.

These data also suggest that coalescence does not enhance the peak vorticity in region III. The peak vorticity here is even less than that of vortex 2 as seen in the last measurement region, namely in figure 11 (*g*), i.e. in phase 4 of pairing. As discussed in I, during the later phases of the pairing process, the diffuse core of vortex 1 is actually seen to recede from vortex 2 while traces of vortical fluid from the former unwind and wrap around the periphery of the latter. This phase of pairing appears to be the one performing 'engulfment' (entrainment) of non-vortical fluid from outside either vortex. The paired vortex becomes progressively more diffuse as it travels farther downstream, and in region IV (figure 11*d*) the measured peak vorticity is quite low compared to that in any of the previous regions.

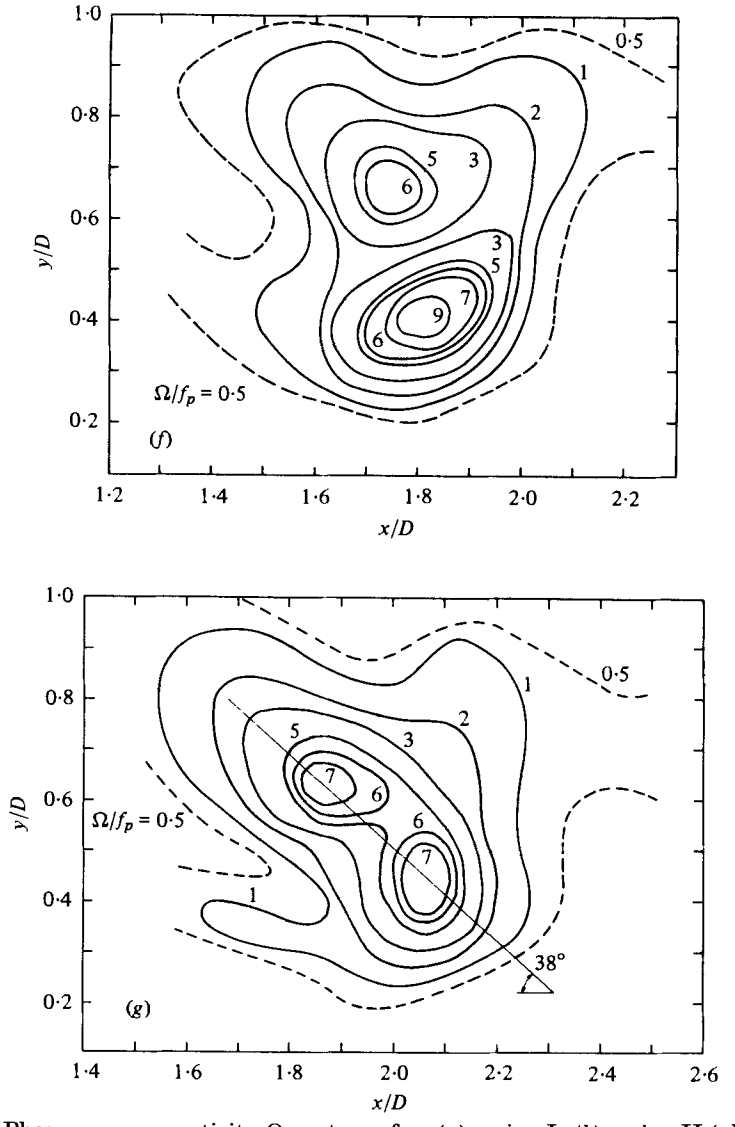

FIGURE 11. Phase-average vorticity Ω contours for: (*a*) region I; (*b*) region II (phase 2), $\Delta\tau = 0$; (*c*) region III; (*d*) region IV; (*e*) region V (phase 1), $\Delta\tau = -2{\cdot}5$ ms; (*f*) region VI (phase 3), $\Delta\tau = 3{\cdot}5$ ms; (*g*) region VII (phase 4), $\Delta\tau = 7{\cdot}5$ ms.

(*a*) *Loss of the peak vorticity.* The measured peak vorticity Ω_p generally drops with increasing downstream distance (figures 11*a–g*). Figure 12 shows Ω_p as a function of x and τ. The peak vorticity of the vortex 2 (the slower-moving outer one of a pair) is considerably higher when it is in region I than when it is in the next measurement region, namely at phase 1 of pairing (in region V, figure 11*e*). Within this distance, the vortex 2 expands slightly in its toroid diameter, increases considerably in the cross-sectional diameter, and is in a state of deceleration due to its interaction with the accelerating vortex 1.

Additional data showing further details of the peak vorticity drop for vortex 2 were

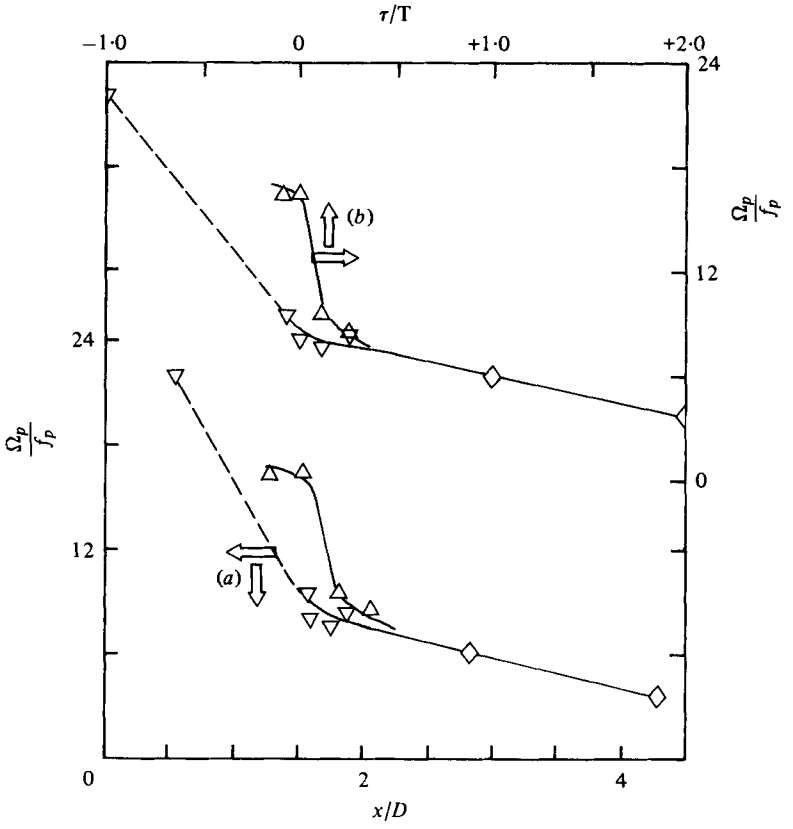

FIGURE 12. Peak vorticity Ω_p as a function of: (*a*) axial distance; (*b*) vortex transit time. △, vortex 1; ▽, vortex 2; ◇, paired vortex.

not taken, but it should be clear that the large overall drop (by 65 % of its initial value) from region I to region V (figures 11*a*, *e*) cannot be due to molecular (viscous) diffusion, since the viscous diffusion time scale $R^2/\nu \approx 24$ s (R being the approximate core radius) is much much larger than the vortex transit time (≈ 25 ms) between regions I and V; that is, viscous diffusion is inconsequential. Thus, although vortex 2 in this region is in a state of being 'stretched' (since the toroid diameter increases), the intense interaction with vortex 1 is probably responsible for the rapid diminution of its core vorticity; this is consistent with the large increase in its core cross-section from region I to region V (see figures 11*a*, *e* and 9*a*).

On the other hand, vortex 1, which is accelerating and undergoing decrease in its toroid as well as cross-sectional diameter, maintains its peak vorticity between phases 1 and 2; this peak value at phase 1 has dropped to only about 70 % from the value at roll-up (the peak vorticity of vortex 1 during roll-up is expected to be the same as that of vortex 2). Between phases 2 and 3, vortex 1 begins decelerating, this process being marked by an abrupt drop of its peak vorticity. The time $\Delta\tau$ elapsed between these two phases is only about 3 ms ($\Delta\tau/T \simeq 10$ %) and within that period, the peak vorticity of vortex 1 has almost halved. Very little decrease is observed farther downstream during passage from phase 3 to phase 4.

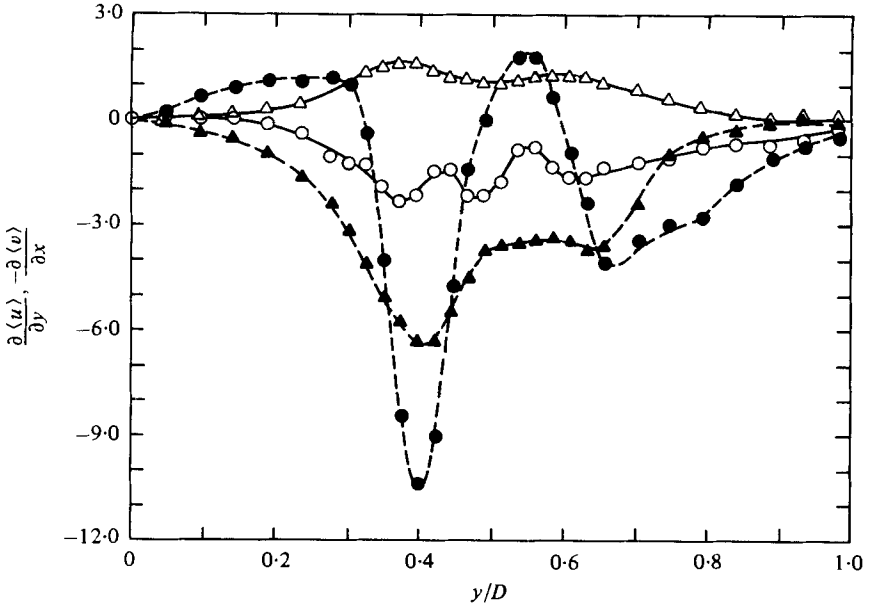

FIGURE 13. Profiles of $\partial\langle u\rangle/\partial y$ (○, ●) and $-\partial\langle v\rangle\partial/x$ (△, ▲) at $x = 9{\cdot}53$ cm (solid symbols) and $x = 11{\cdot}75$ cm (open symbols). Data are non-dimensionalized by the excitation frequency f_p.

The abrupt drop of the peak vorticity of vortex 1 from phase 2 to 3 is probably associated with its sudden deceleration and relaxation to a larger core diameter as it passes through the radial configuration (figures 11*b*,*f*), as well as the onset of large turbulence due to transition. These data are thus consistent with the visual observation that vortex 1 undergoes a sudden transition (marked by an explosive diffusion of the smoke tracers) soon after it passes through the radial configuration. This thus marks the most dramatic change in the large-scale vorticity during the pairing event.

(*b*) *Braids.* All the vorticity contours shown in figures 11(*a*, *b*) appear as concentrated lumps with no significant vorticity in the braids between two vortical structures. In figure 13, $\partial\langle u\rangle/\partial y$ and $-\partial\langle v\rangle/\partial x$ as functions of y are shown for $x = 9{\cdot}53$ and $11{\cdot}75$ cm, the former x station being midway between the vortices in regions I and II while the latter corresponds to the location of the centres of the two vortices in region II. Note that $\partial\langle u\rangle/\partial y$ and $-\langle\partial v\rangle/\partial x$ for $x = 11{\cdot}75$ cm are of the same sign almost everywhere and thus the total vorticity is higher in magnitude than either of these two components. But the magnitudes of $\partial\langle u\rangle/\partial y$ and $-\partial\langle v\rangle/\partial x$ at $x = 9{\cdot}53$ cm are not only low but also cancel each other, thus producing much lower vorticity everywhere between two adjacent vortices. That is why the contours of the lowest value of Ω/f_p (i.e. 0·5) in the intermediate regions have too much scatter (shown by dotted lines in figures 11*a*–*g*) to show any clear boundaries of the braids.

The roll-up of the shear layer is a mechanism for accumulation of vorticity in lumps. The phenomenon of accumulation of vorticity in lumps, even in an inviscid vortex sheet (i.e. shear layer), is a simple consequence of the sinusoidal undulation of the layer due to its (inviscid) instability. Consider a growing sinusoidal displacement of a uniform vortex sheet; at locations of maximum slope, half-wavelengths apart, the growing sinusoidal displacement will alternately augment and diminish vorticity.

The induced velocities associated with this vorticity perturbation will accelerate the accumulation process (Batchelor 1970, p. 516). The result is the roll-up of the shear layer into vortical lumps one wavelength apart, connected by thin braids. The induced motion associated with the like-signed vortex trains will draw more and more vortical fluid into the vortex lumps away from the braids. In a vortex train in a mixing layer of characteristic velocity scale U_e, the circulation per wavelength $\Gamma = U_e \lambda$ is constant. If the wavelength is divided into two parts, one containing a vortex and the rest the adjoining braid, then the total of circulations Γ_b and Γ_c around the braid and the vortex, must equal Γ, i.e. $\Gamma_b + \Gamma_c = \Gamma$. The continued rotation of the like-signed adjoining vortical structures will stretch the intervening braid and pull vortical fluid away from the braid into the vortical lumps and, thus, increase Γ_c with time. Hence Γ_b must progressively decrease. If one assumes that the vorticity diffusion transverse to the braid is strong enough to disallow rapid decrease in the braid thickness, it then follows that the braid vorticity will progressively diminish.

Corcos & Sherman's (1976) analysis for a gravitationally stable stratified shear layer demonstrates that braid vorticity is steadily depleted by advection to the cores, but is replenished by baroclinic generation. Based on this analysis, they concluded: 'In the uniform-density or barotropic case, the terminal state is one in which vorticity of the braids is totally depleted.' Their analysis thus supports the low braid vorticity measured by us.

3.3. *Jitter, flow reversal and contour distortions*

The roll-up, pairing, and passage of paired vortices even under the excitation is not exactly periodic in space and time. There are small deviations from periodicity due to dispersion in convection velocity, shape, size, orientation, etc. which can be observed visually with the help of a stationary marker and stroboscopic illumination of the flow (see I); these deviations will be denoted as 'jitter'. The effect of the jitter would be to smear out the spatial gradients of the different phase-averaged flow properties, as well as to contribute to the phase-average turbulence intensities in regions of large gradients.

The jitter of the vortices generally increase with downstream distance but vortex 1 assumes large uncertainties in its arrival time at $x/D = 1{\cdot}5$ while 'zooming' through vortex 2. Since the reference probe, used to obtain the triggering signal, was located at $x/D = 1{\cdot}5$ (on the centre-line), the relative jitter between the triggering signal and the vortex arrival time was the least for vortex 1 at this location. But this relative triggering signal jitter was appreciable for vortex 2 at the same axial location (estimated to be about 0·2 cm by flow visualization experiments, or about 1 ms), for vortex 2 in region I, and for the paired vortex farther downstream.

The 'dip' in the vorticity contours, especially on the low-velocity side, observed nearer to the exit is a result of the combined effects of the triggering signal jitter and flow reversal. Let us consider the effect of the triggering signal jitter first. Consider the two pairing vortices as shown in figure 14(*a*) at three adjacent phases *A*, *B* and *C*. Also assume that measurements in phase *B* are desired. Owing to jitter in the passage of vortex 1, trigger will occur randomly between phases *A* and *C*. But since the triggering signal is obtained from the reference probe placed close to the (inner) vortex 1, the physical location of the (outer) vortex 2 will vary from trigger to trigger as shown in figure 14(*b*). Consequently, vorticity measured at measurement point 2 (in phase *B*)

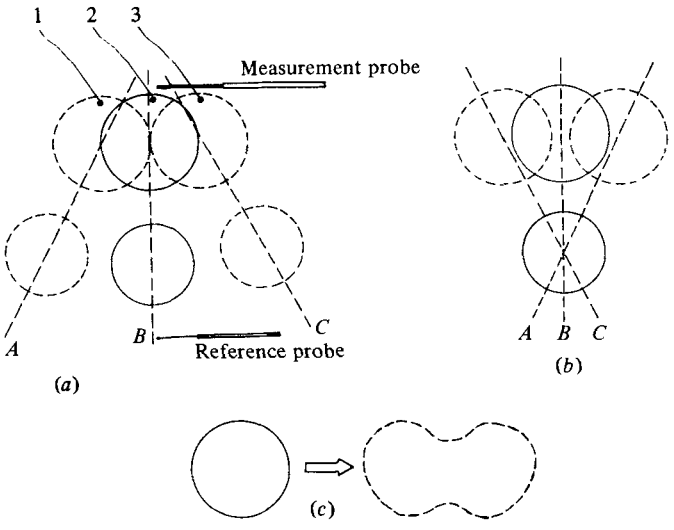

FIGURE 14. Contour distortion due to triggering signal jitter induced by vortex 1.

will be diluted by phases A and C. On the other hand, at either of the measurement points 1 and 3 in phase B, measured vorticity will be weighted by phases C or A. Furthermore, the probability of occurrence of either A or C is larger than B owing to the time-dependent convection velocity of vortex 1; see I. (Indeed, if the flow in phase B is illuminated with external trigger, vortex 1 appears more often at either phase A or C rather than B.) Therefore, distortions of a vortex cross-section (figure 14*c*) would be expected. This should explain, at least partially, the observed 'dips' in regions II and VI, and also in regions I, V and VII.

As explained before, the relative jitter for vortex 1 is least in regions II or VI, which should explain why such a 'dip' is not observed for vortex 1 (on the high-speed side) in these regions. However, if vortex 1 is sufficiently away from $x/D = 1{\cdot}5$, the effect is expected to occur on the high-speed side; this is indeed observed in region V (see figure 11*e*). In region I, the effect of the relative jitter on the contour distortion on the high-speed side is not obvious owing to the 'folding' of the contours. On the other hand, the above effect is less pronounced in regions III and IV, where the jitter, not only in arrival times but also in shape, size, orientation, etc., presumably become more pronounced and no clear 'dips' are observed on either the low-speed or the high-speed side of the vortices (figures 11*c*, *d*). Obviously, the contour distortion in vortex 2 in the regions nearer to the exit could be lessened if the reference probe were placed close to vortex 2 (e.g. at $x/D = 1{\cdot}5$ but outside the shear layer). This was not done because the signal at the outer edge of the shear layer is not 'clean' and also because such a scheme would grossly distort vortex 1 in the regions of pairing.

Flow reversal. Further investigations revealed that the flow on the low-speed side undergoes reversal (i.e. directed upstream). Thus, at some phases during the passage of the vortices, the hot wire being insensitive to flow reversal, the instantaneous measurements of the velocity vector direction and the vorticity would be in error. This measurement error contributed further to the contour distortions on the low-speed side.

Flow reversal is illustrated in figure 15 (plate 2) by the two oscilloscope signal traces from a hot-wire–cold-wire pair sensor located at $x/D = 0{\cdot}6$ at the radial location where $U/U_e = 0{\cdot}10$. The cold wire was located about 1 mm upstream of the hot wire, normal to the latter and placed at the latter's mid-length. The cold wire was about 1 mm long, 1 μm in diameter and operated at a very low overheat so that it was sensitive to temperature only. The hot wire was about 1 mm long and 5 μm in diameter and operated at an overheat ratio of 0·8. Both were etched Wollaston wires made of 90 % Pt and 10 % Rh. The top (inverted) trace from the cold wire shows temperature spikes produced by the wake of the hot wire, unambiguously representing the instants of flow reversal. The unique connexion of the (negative) spikes in the cold-wire signal with flow reversal was confirmed by the fact that the cold-wire signal showed absolutely no spike at any radial location, when only the hot-wire current was turned off. Note that the positive spikes in the velocity signal, corresponding to the negative spikes in the cold-wire signal, represent negative velocity, but are rectified by the hot wire. (Professor R. A. Antonia's help in the flow-reversal experiments is deeply appreciated.)

The flow reversal was found to occur only when the probe was located at a radial position outside the corresponding vortex centre at that location. Study at different x and y in an unperturbed circular jet showed that reversal is a consequence of large-scale structures and progressively becomes weaker with increasing x. In the jet under excitation, the flow reversal commenced at $U/U_e \gtrsim 0{\cdot}30$ (occasional at this location); with increasing radius the strength of the spikes increased to a maximum at about $U/U_e \simeq 0{\cdot}05$ and then it progressively dropped off. Measurements along the $U/U_e = 0{\cdot}10$ line revealed that it is more pronounced and frequent closer to the exit, e.g. in regions I and II where the vortices are more energetic and becomes progressively less frequent with increasing x, e.g. in regions III and IV. Note that the spikes in the temperature signal are alternately weak and strong due to the different lateral positions and possibly different strengths of the alternate vortices 1 and 2 passing by the probe. Furthermore, the flow reversal phenomenon was not exactly periodic because of jitter and the amplitude of the temperature spikes varied widely with time (see figure 15).

Consider now the measurement points on the low-speed side on a radial line AB passing through the vortex centre (figure 16*a*). On this line, the phase-average $\langle v \rangle$ should be zero but, around point B, the measured $\langle u \rangle$ velocity would be in error in sign due to the flow reversal. Specifically, the actual $\langle u \rangle$ profile along line AB, shown by the solid line in figure 16(*b*), would be measured as the dotted line from point C outwards. Consequently, a vorticity contour line on the low-speed side would be shifted towards the jet centre-line (figure 16*c*). Since the reversal phenomenon occurs only over a short time, the above effect would be limited presumably around point B (figure 16*a*), thus explaining the observed contour distortions. Since the flow reversal would not explain the contour distortions observed on the high-speed side (e.g. in figure 11*e*), it is concluded that the observed distortions were due to the combined effects of the triggering signal jitter and the flow reversal.

3.4. *Role of the vortical structures in the flow dynamics*

The contours of constant $\langle v \rangle$ for regions I–IV are shown in figures 17(*a*)–(*d*). The plus symbol in each figure roughly locates the vortex centre, determined from the vorticity contours. Solid lines represent positive values of $\langle v \rangle$ (representing motions

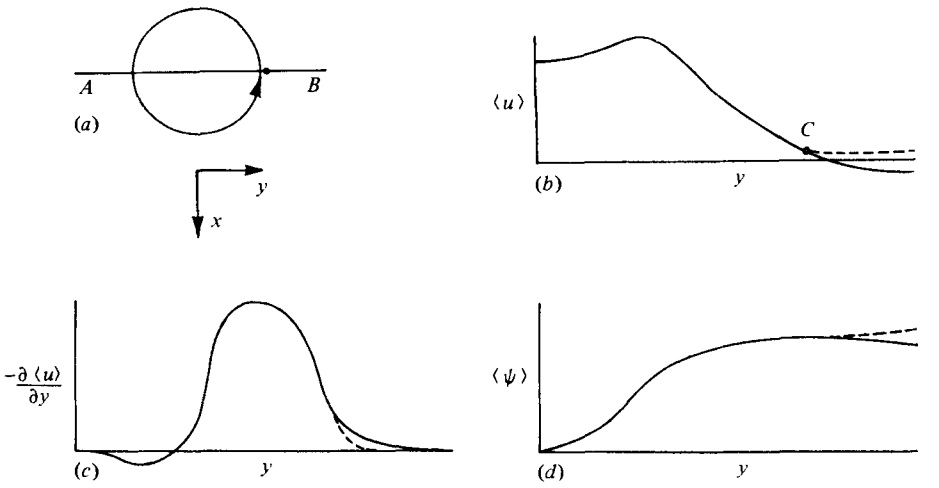

FIGURE 16. Explanation for measurement errors due to flow reversal.

away from the jet centreline) while dashed lines represent inward motions. These contours suggest that entrainment of non-vortical fluid from outside the jet occurs mainly at the trailing edges of the vortical structures. Notice also that the regions encompassing negative $\langle v\rangle$ become progressively larger than those encompassing positive $\langle v\rangle$ as the structure travels downstream. Thus in region IV, the vortical structure mainly brings outside fluid inwards.

The $\langle v\rangle$ contours provide a clearer understanding of the transverse motions than provided by the staggered profiles in figure 8. The $\langle u\rangle$ contours are not shown partly to conserve space and also partly because the large transverse gradients of the mean axial velocity will not allow the effect of the vortices on $\langle u\rangle$ to be seen clearly. However, the correlation $\langle uv\rangle$ contours are presented in figures 18(a)–(g) for regions I–VII, respectively. As in figure 17, positive values are shown by solid lines while negative values are shown by dashed lines. Figures 18(a)–(c) show clearly that the values of the correlation have regions of alternate positive and negative distributions in x. On the upstream front of a vortex, large negative correlations are encountered, while on its downstream side large positive values are found. This is consistent with the flow visualization pictures showing a vortical lump pushing the high-speed jet core fluid outwards near the leading end but pulling back external fluid at the rear of the vortical structure.

Note that in region I, while only one positive and one negative region occurred in the $\langle v\rangle$ contours (figure 17a), the $\langle uv\rangle$ contours (figure 18a) show two additional regions farther downstream – showing that the spatial periodicity in $\langle uv\rangle(x)$ is double that of $\langle v\rangle(x)$. This can be explained qualitatively: $\langle u\rangle(x)$ is symmetric and $\langle v\rangle(x)$ is antisymmetric about the vortex centre (see figures 7 and 8), thus if $\langle u\rangle(x)$ is represented by $A\cos 2\pi x/L$ and $\langle v\rangle(x)$ by $B\sin 2\pi x/L$, $\langle uv\rangle(x)$ will be $AB\sin 2\pi x/\frac{1}{2}L$ (i.e. antisymmetric about the vortex centre, as was found to be the case in figure 10b). This shows that the wavelength in $\langle uv\rangle(x)$ will be halved, thus accounting for the two additional positive and negative contour regions in figure 18(c). Similar halving of the wavelength in the $\langle uv\rangle(x)$ data can also be noticed in region I. The contours are com-

plicated in the regions of pairing, i.e. in figures 18(*b*), (*e*), (*f*) and (*g*). In region IV (figure 18*d*), the $\langle uv \rangle (x)$ values are obviously too low to exhibit such alternate positive and negative correlation regions.

Note that the alternating positive and negative coherent Reynolds stresses associated with the pairing vortices (figures 18*b*, *e*, *f*, *g*) suggest that the time-average Reynolds stress and production can be negative. As shown in I, production can be negative over an appreciable region. Thus even though it contrasts gradient transport hypotheses and turbulence modelling theories, negative production can be explained by considering coherent structure interactions.

With increasing x the vortices become weaker and the contribution of $\langle u_r v_r \rangle$ to the total correlation $\langle uv \rangle$ become pronounced. Nearer to the exit, e.g., in regions I and II, $\langle u_r v_r \rangle$ is very small, the total correlation $\langle uv \rangle$ being primarily due to the large-scale organized vortices; i.e. $\langle uv \rangle \simeq \langle u_p v_p \rangle$. In region III, $\langle u_r v_r \rangle$ values are still quite low in magnitude compared to $\langle uv \rangle$ values but, in region IV, $\langle u_r v_r \rangle$ is found to be comparable or even higher than $\langle u_p v_p \rangle$. Figures 19(*a*)–(*c*) show variations of $\langle uv \rangle$ and $\langle u_r v_r \rangle$ as functions of y for regions II, III and IV at the leading ends of the coherent vortical structures. As shown in (*a*), the values of $\langle u_r v_r \rangle$ in region II are in the 'noise' level compared to values of $\langle uv \rangle$. Similarly, very small values of $\langle u_r v_r \rangle$ are generally found in the measurement regions I, V, VI and VII (not shown). In region III, however, where turbulence has set in in the paired vortex core, values of $\langle u_r v_r \rangle$ are still low but are no more negligible; see figure 19(*b*). Notice that the ordinate scale in (*b*) is 10 times that in (*a*); thus the phase-average correlation magnitudes in region III are generally an order-of-magnitude less than those in region II. Figure 19(*c*) shows that, in region IV, $\langle u_r v_r \rangle$ and $\langle u_p v_p \rangle (= \langle uv \rangle - \langle u_r v_r \rangle)$ values are comparable; that is, transport by organized and random motions are equally important.

Part of the measured $\langle u_r v_r \rangle$, especially in the downstream regions, are believed to be contributed by the triggering-signal jitter (see § 3.3). In a recent study of vortex shedding from a cylinder, using phase-averaging techniques, Cantwell & Coles (1978, private communication) found values of $\langle u_r v_r \rangle$ comparable to $\langle u_p v_p \rangle$ everywhere in the flow field. In spite of their suggestion to the contrary, the large $\langle u_r v_r \rangle$ values found by them may be due partly to the phase jitter of the structure arrival times.

Zone-average coherent Reynolds stress. Figures 18(*b*), (*e*), (*f*) and (*g*) reveal that the negative correlation regions are marked by lower magnitudes than those in the positive regions, suggesting an average positive correlation over the passage of the pairing vortices. Browand & Wiedman (1976) showed that the average correlation coefficient (averaged in time at each y) was in general higher during the passage of a pair of coalescing vortices than during the passage of an already paired vortical structure. A parallel effort was undertaken here to compute average correlation for each y over a certain x range. Thus, while Browand & Wiedman's data show average correlation coefficient for a certain x over a time span covering the passage of the vortical structures, the following data represent correlation at a certain instant of time (or phase) but averaged over an x range encompassing the vortical structures. In view of the rapid temporal changes in the coherent momentum transport, these data should be more meaningful. The zone-average correlation is defined as

$$\widehat{u_p v_p} = \left[\frac{1}{x_2 - x_1}\int_{x_1}^{x_2} \langle u_p v_p \rangle \, dx\right] \Big/ (u'v')_{\max}, \tag{3.1}$$

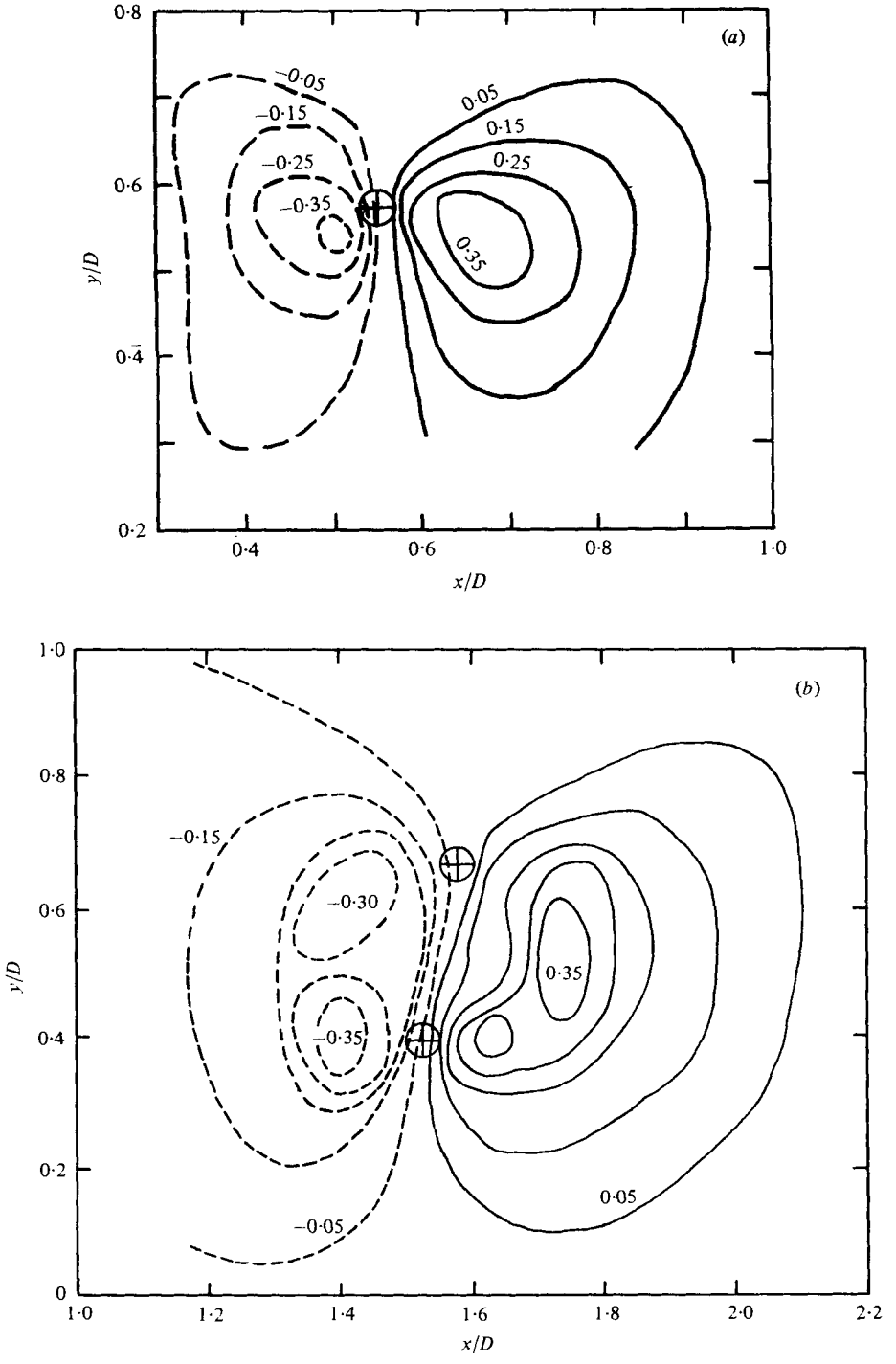

FIGURE 17 (*a*, *b*). For legend see facing page.

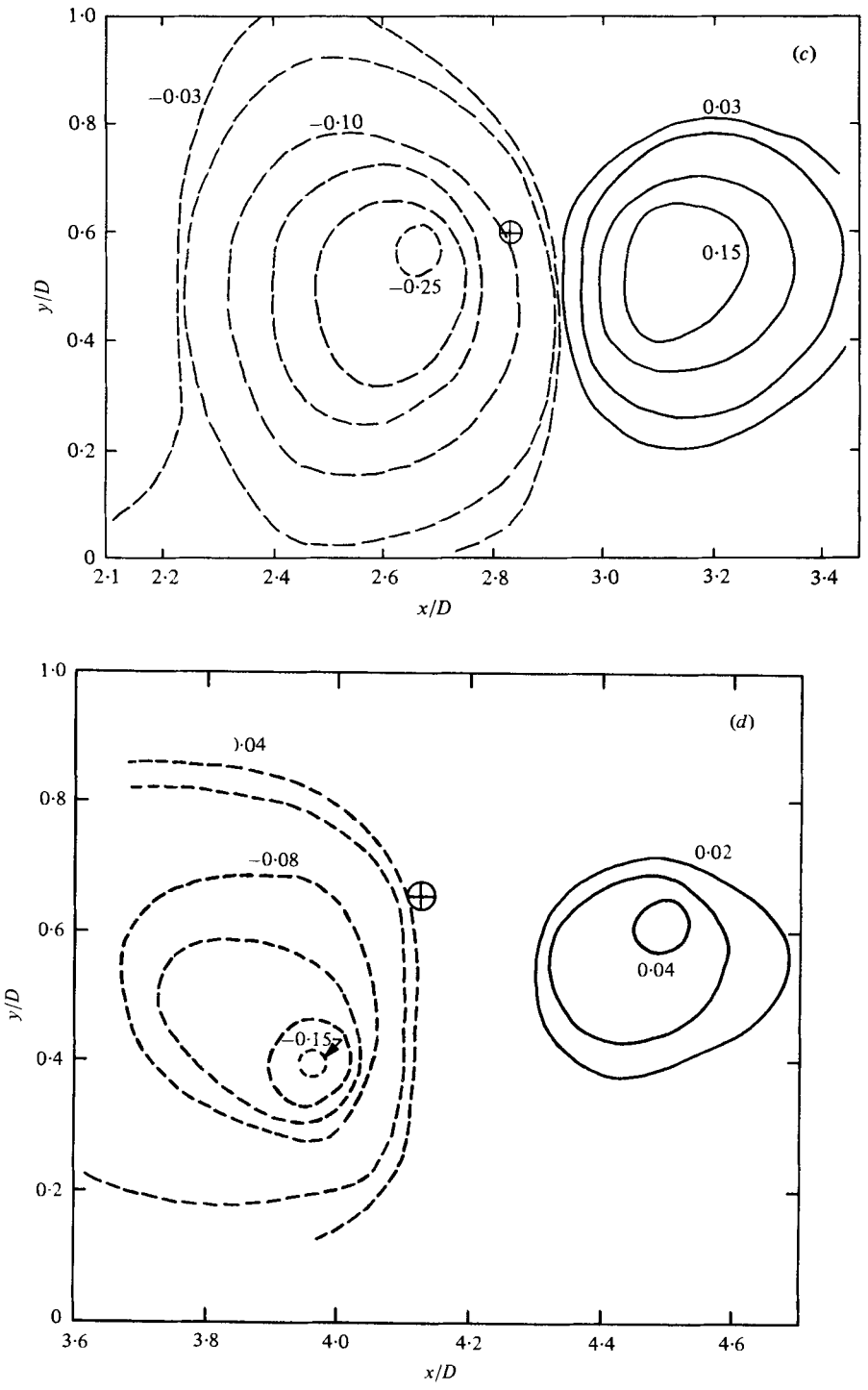

FIGURE 17. Contours of constant $\langle v \rangle / U_e$ for: (*a*) region I; region II; (*c*) region III; (*d*) region IV.

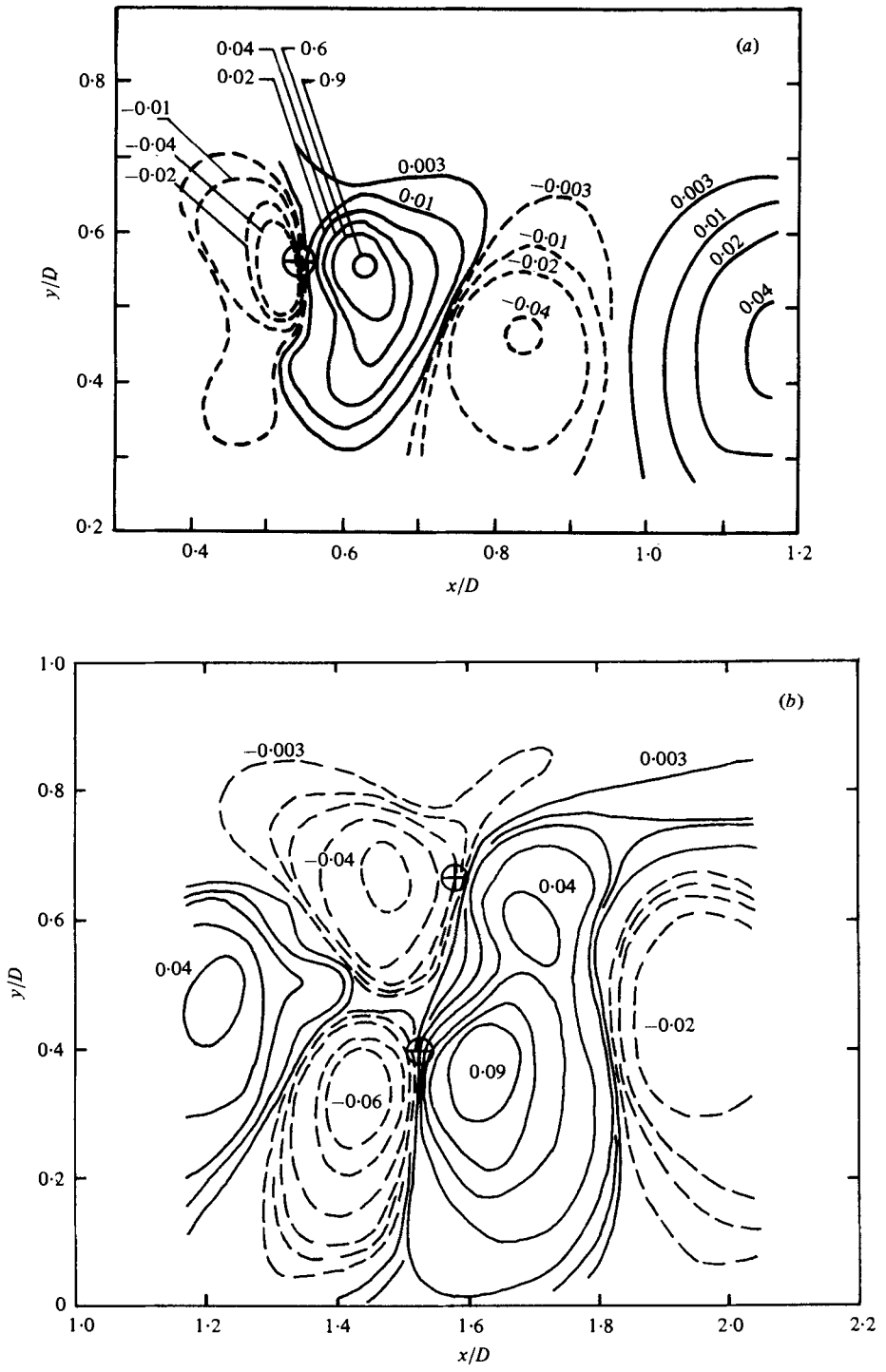

FIGURE 18 (*a*, *b*). For legend see page 521.

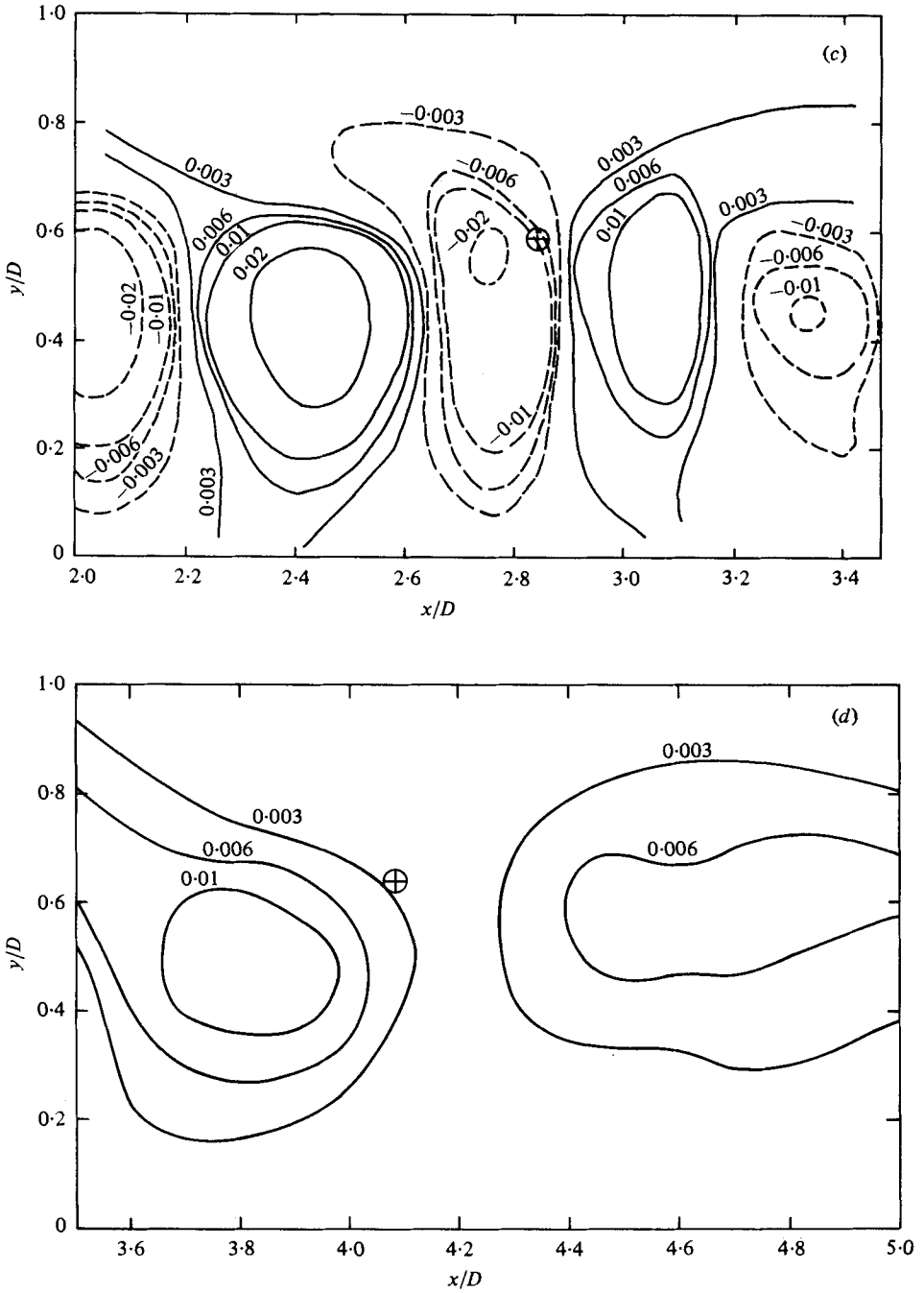

FIGURE 18 (*c*, *d*). For legend see page 521.

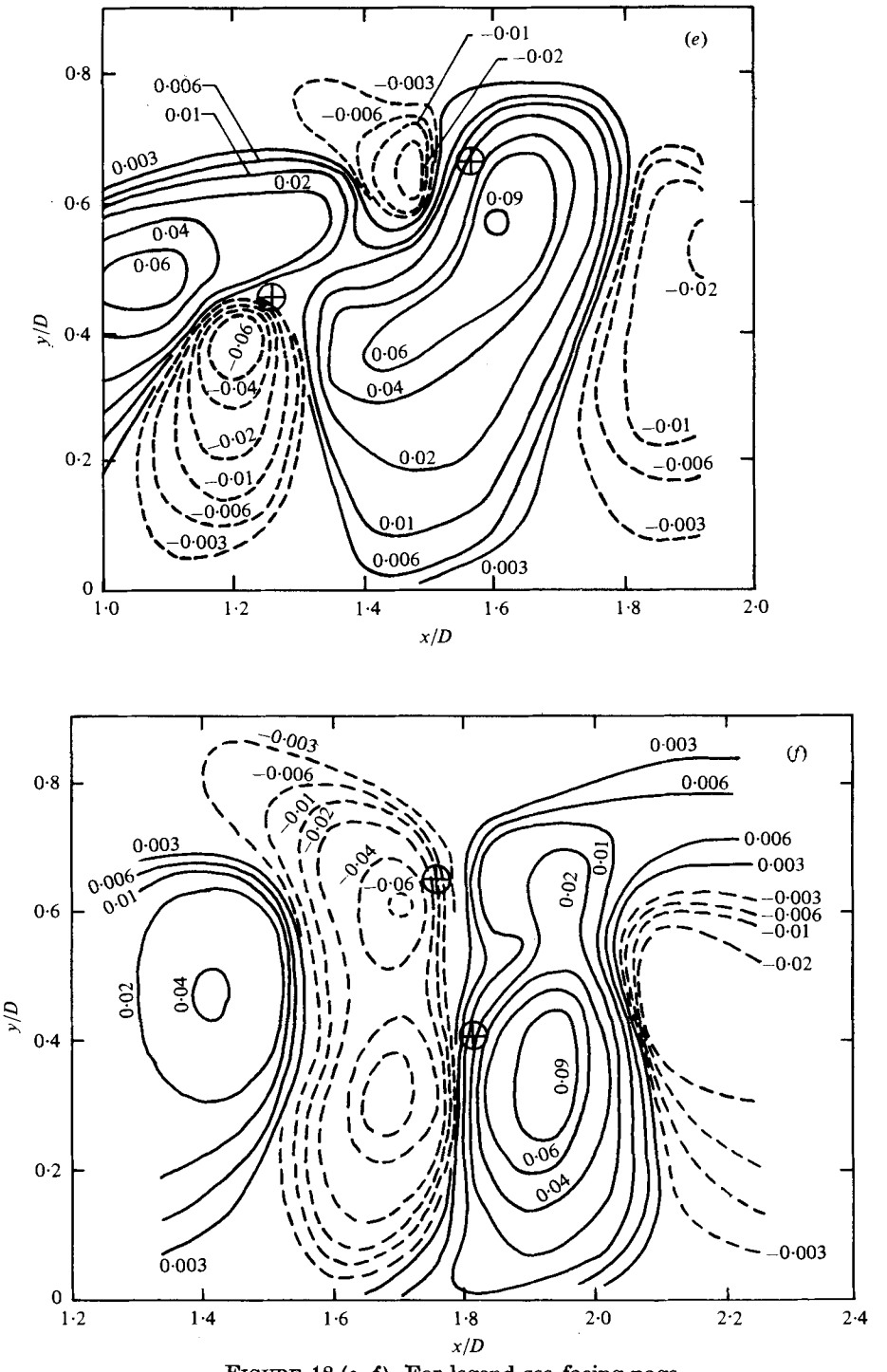

FIGURE 18 (*e*, *f*). For legend see facing page.

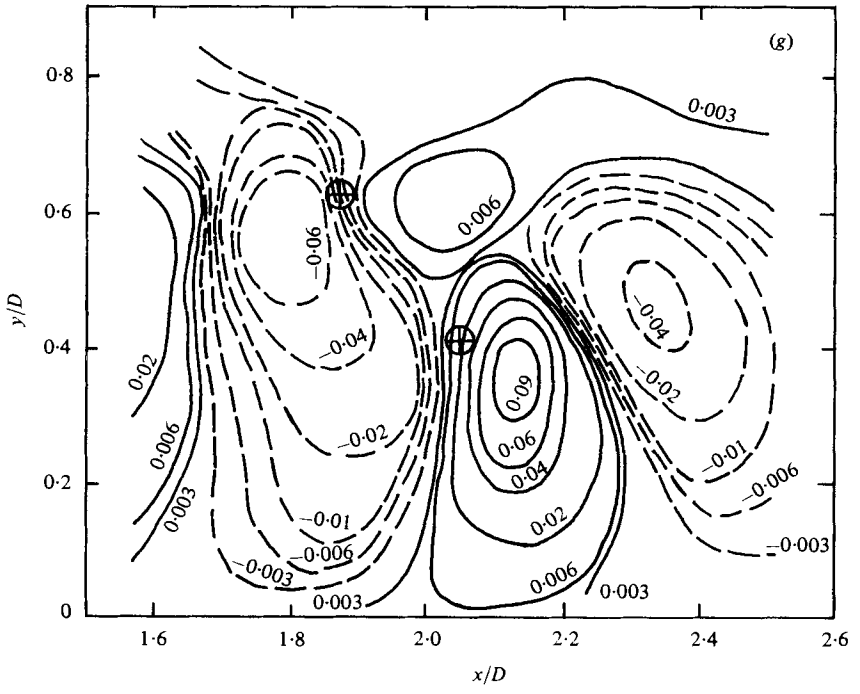

FIGURE 18. Contours of constant $\langle uv\rangle/U_e^2$ for: (*a*) region I; (*b*) region II; (*c*) region III; (*d*) region IV; (*e*) region V; (*f*) region VI; (*g*) region VII.

where u' and v' are the time-average turbulence intensities; thus normalization was done by a constant quantity for all y in a particular region. For each region under study, the range (x_1, x_2) was chosen to include only the $\Omega/f_p = 1{\cdot}0$ contour and was kept constant at all y. The $\widehat{u_p v_p}$ *vs.* y/D data for regions I–IV are shown in figure 20. The maximum values of $u'v'/U_e^2$, i.e. normalization factors, for the regions I–IV were 0·0657, 0·0627, 0·0553 and 0·0394, respectively. The value of $\widehat{u_p v_p}$ is large when the two vortices are in the process of pairing but is almost zero for regions I, III and IV, where only one vortical structure is present. Notice that averaging over only a few (i.e. 8–12) x stations, resulted in considerable scatter in the data.

Even though these data and those of Browand & Wiedman (1976) are based on different approaches, the implications are in qualitative agreement. These data suggest that correlation over a single vortical structure, no matter how it is formed (say, in regions I, III, IV), is much lower than that during pairing. It should be emphasized that the correlation values shown here are dependent on the bound (x_1, x_2) chosen for the averaging. This can best be appreciated from the $\langle uv\rangle$ contours as shown in figure 18. Since $\langle u_p v_p\rangle$ is alternately positive and negative, shift of and/or change in the extent of the range (x_1, x_2) will affect the value of $\widehat{u_p v_p}$.

Similar zone-average correlations for the regions V, II, VI and VII reveal the relative importance of different phases in the pairing process. Figure 21 shows $\widehat{u_p v_p}$ *vs.* y for phases 1, 2, 3 and 4 of the pairing event. As is evident, phase 1 exhibits maximum zone average correlation of all the four phases. The correlation peaks are the lowest in phase 4; when integrated in y, this phase will produce the least average correlation.

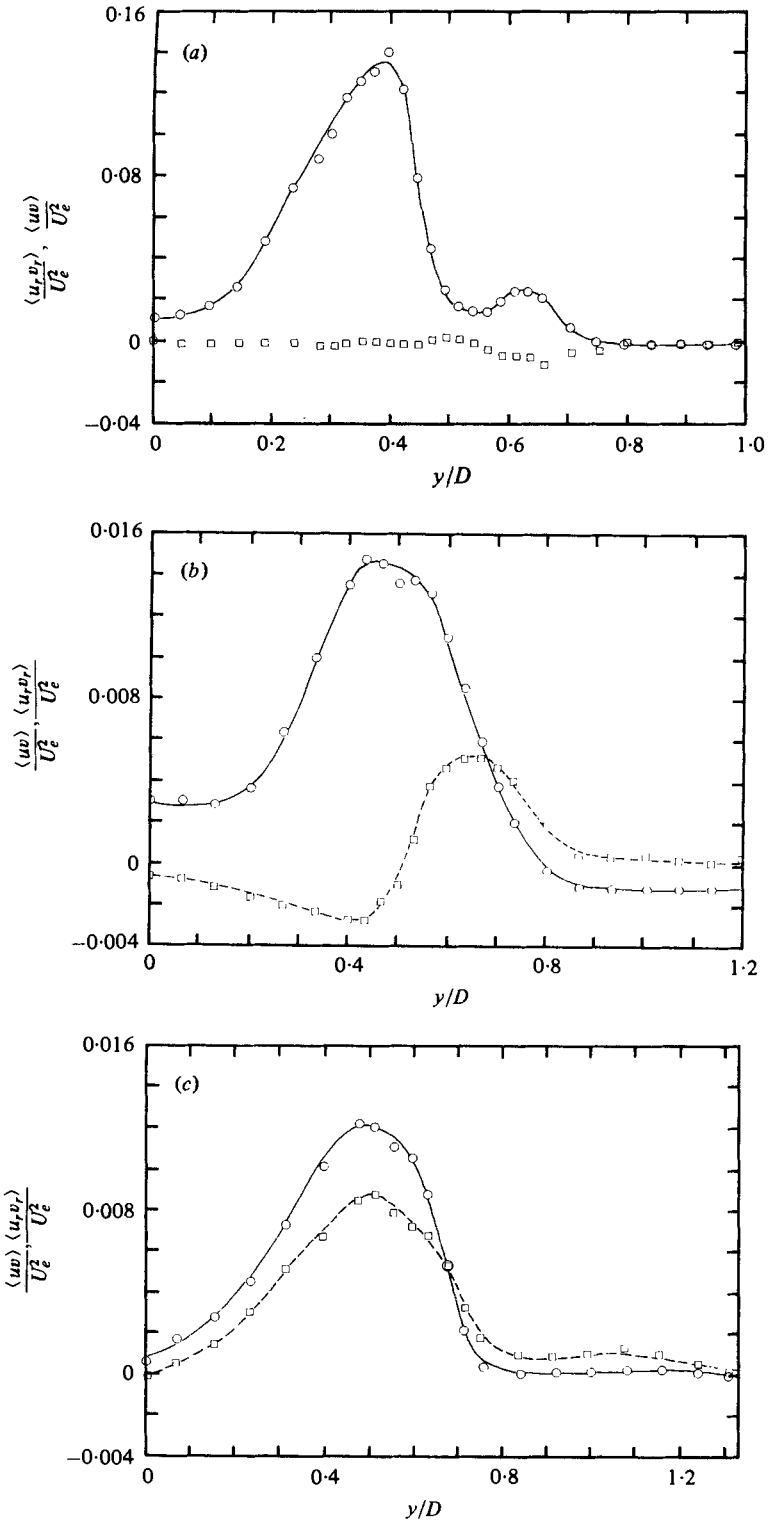

FIGURE 19. Profiles of the phase-average total Reynolds stress (○) and the background turbulence Reynolds stress (□) for: (*a*) region II at x = 12·38 cm; (*b*) region III at x = 22·86 cm; (*c*) region IV at x = 29·21 cm.

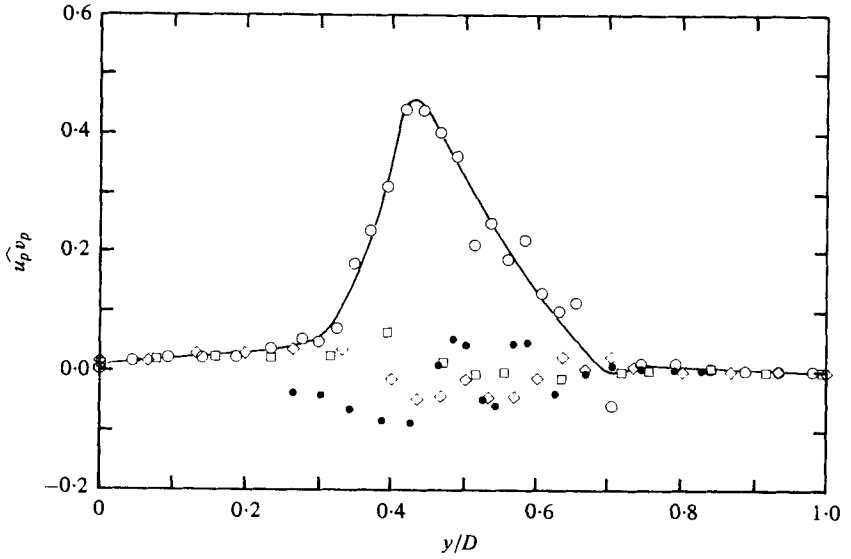

FIGURE 20. Profiles of the 'zone-average' coherent structure Reynolds stress $\widehat{u_p v_p}$ for: ●, region I; ○, region II; ◇, region III; □, region IV.

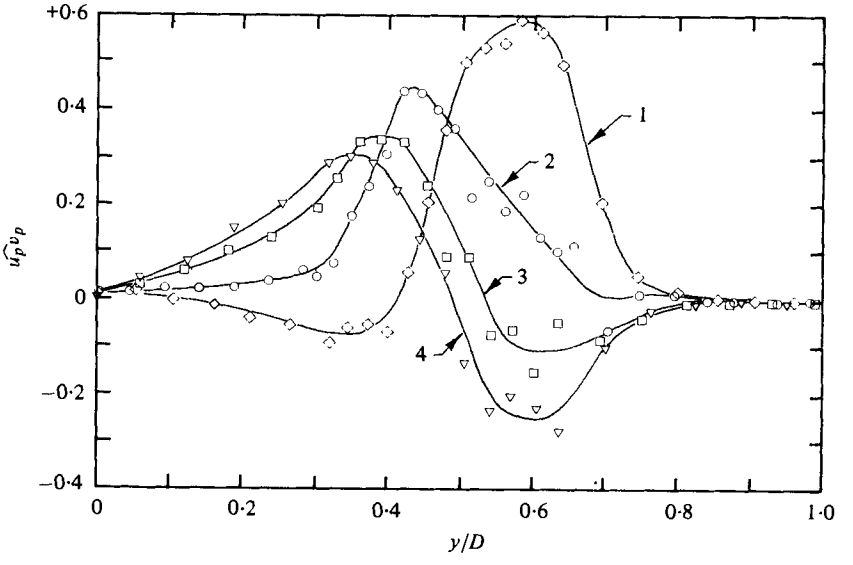

FIGURE 21. Profiles of $\widehat{u_p v_p}$ for the different phases of pairing: ◇, phase 1 (region V); ○, phase 2 (region II); □, phase 3 (region VI); ▽, phase 4 (region VII).

(Note that the normalizing factors $(u'v')_{\max}$ were approximately the same for the four phases; it decreased somewhat from phase 1 to phase 4, the maximum decrease being within 3 %.)

Thus, it is concluded that maximum transverse transport of the $\tilde{u}$ momentum occurs during the early phases of the pairing process. It should be mentioned here that the pairing event captured in the plane mixing-layer study by Browand & Wiedman (1976) represents an average over a *range* of phases in the pairing process. Their study, however,

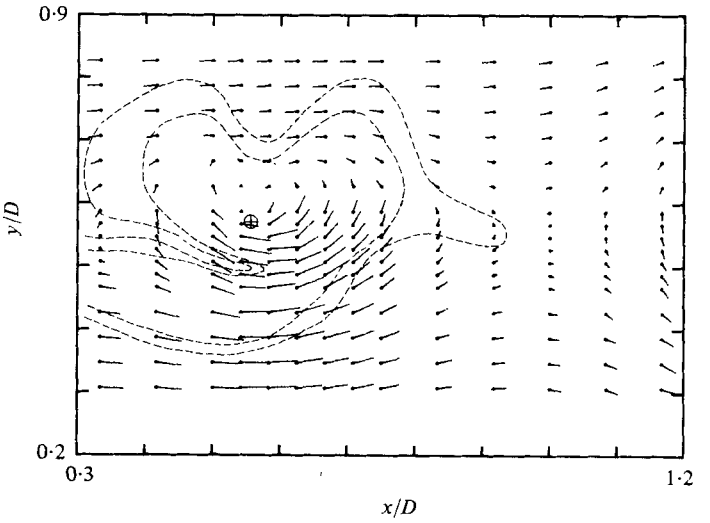

FIGURE 22. Distribution of the velocity vectors in region I with a reference frame velocity $U_{\text{ref}} = 0{\cdot}4U_e$.

does not provide phase-dependent information, owing to the use of the Taylor hypothesis in obtaining spatial distributions of properties from time traces. Following that approach, evolution of the coherent structure at different phases cannot be unveiled (Zaman & Hussain 1981).

3.5. *Phase-average streamlines*

In an effort to understand further the coherent structure dynamics, phase-average streamlines are discussed in this section. From the $(\langle u\rangle, \langle v\rangle)$ data in the (x, y) plane, it is possible to draw the phase-average streamlines at the specific phases under consideration. The equation of a streamline being $\mathbf{u} \times \mathbf{ds} = 0$, the slope of the phase-average streamline ψ_p at any location $\mathbf{x}$ is given by $dy/dx = \langle v\rangle/\langle u\rangle$. Thus the phase-average streamlines at any phase can be drawn from the spatial distribution of the velocity vectors $(\langle u\rangle, \langle v\rangle)$ by the method of isoclines. Interpretation of the flow dynamics by streamlines, especially those of vortical motions, is not straightforward because the streamlines are not invariant under Galilean transformation. Thus, with respect to the laboratory co-ordinates, the average streamlines in any of the measurement regions would be essentially smooth, almost straight lines showing no coherent structure. Only when the reference frame is translated with the convection velocity of the vortices, would the vortical motion be apparent. The problem is further compounded by the relative motions within the structure itself.

Figures 22–25 show the spatial distributions of the phase-average velocity vectors in the regions I–IV respectively, at the phase under consideration. In each figure, the velocity-vector origins are denoted by the dots, the directions by the orientations of the lines from the dots, and the magnitudes by the line lengths. In figure 22, the reference frame velocity used is $0{\cdot}4U_e$ which is the convection velocity of the type 2 vortex in this region (see I). A picture of the vortex cross-section, not unlike the vorticity contours, clearly emerges from the velocity vectors. In order to compare the streamline patterns with the structure boundary, the vorticity contours ($\Omega/fp = 1{\cdot}0$ and $2{\cdot}0$ with the vortex centres denoted by the symbol $\oplus$) are also shown in this figure

as dotted lines. Defining the structure boundary by the iso-vorticity contours seems appropriate since the coherent structures are vortical and also since they are invariant under Galilean transformation. Note that the structure centre denoted by the streamlines in figure 22 nearly coincides with that denoted by the peak vorticity.

The region II involves two vortices in intense relative motion, and interpretation of the streamline pattern needs care. If the velocity vectors are drawn with respect to the laboratory frame, no vortical motion will be evident from the smooth parallel streamlines in that frame. Figures 23(*a*)–(*c*) show the velocity vector patterns with the co-ordinates convected downstream with: (*a*) the streamwise velocity of vortex 1 ($1{\cdot}25\,U_e$), (*b*) the streamwise velocity of vortex 2 ($0{\cdot}35U_e$), and (*c*) the average streamwise convection velocity $0{\cdot}8U_e$ of the two; see I. Note that in figure 23(*a*), vortex 2 is completely obliterated and the closed streamlines appear only around the vortex 1 centre. On the other hand, in figure 23(*b*), closed streamlines appear only around the centre of vortex 2, and vortex 1 remains hidden. The much higher convection velocity of vortex 1 influences the streamlines in the latter figure, resulting in an elongated and somewhat elliptical closed contours over vortex 2. When the average of the two convection velocities are used for co-ordinate translation (figure 23*c*), neither one of the vortex centres is clear.

The convection velocities of the paired vortex are used to show similar streamline patterns in regions III and IV in figures 24 and 25, respectively, with the vorticity contours superimposed on them. Even though regions III and IV are after vortex pairing and transition, especially in region IV where visualization experiments hardly show any coherent structure, the phase-average streamlines clearly reveal the vortical motions. Furthermore, there being a single vortical structure in either of these two regions, and the reference frame being convected downstream with the velocity of the paired vortex, the streamline patterns agree fairly with the vorticity contours. The structure aspect ratio as well as its spacing between regions III and IV very closely agree with the naturally occurring 'average' structure educed by Yule (1978). Yule found the spacing to be roughly $1{\cdot}3D$; the distance between the structures in regions III and IV is about $1{\cdot}25D$.

In order to provide an example of the nature of the streamlines drawn from the spatial distributions of $(\langle u\rangle, \langle v\rangle)$, figure 26 shows the phase-average streamlines ψ_p corresponding to the case of figure 23(*a*).

3.6. *Phase-average pseudo stream functions*

It is possible to compute the stream functions at a particular phase from the spatial distributions of the phase-average streamwise velocity $\langle u\rangle(x, y)$ alone. In the near flow field of the axisymmetric jet, the phase-average velocity field can be considered axisymmetric. Thus for incompressible motion, the continuity equation in the cylindrical co-ordinates (x, r, α) corresponding to the velocity components (u, v, w) is

$$\frac{\partial\langle u\rangle}{\partial x}+\frac{1}{r}\frac{\partial}{\partial r}(r\langle v\rangle) = 0, \tag{3.2}$$

from which it follows that there exists a scalar function $\langle\psi\rangle(x, r)$ such that

$$\langle u\rangle = \frac{1}{r}\frac{\partial\langle\psi\rangle}{\partial r}; \quad \langle v\rangle = -\frac{1}{r}\frac{\partial\langle\psi\rangle}{\partial x}, \tag{3.3}$$

and that

$$d\langle\psi\rangle = r\langle u\rangle\,dr - r\langle v\rangle\,dx, \tag{3.4a}$$

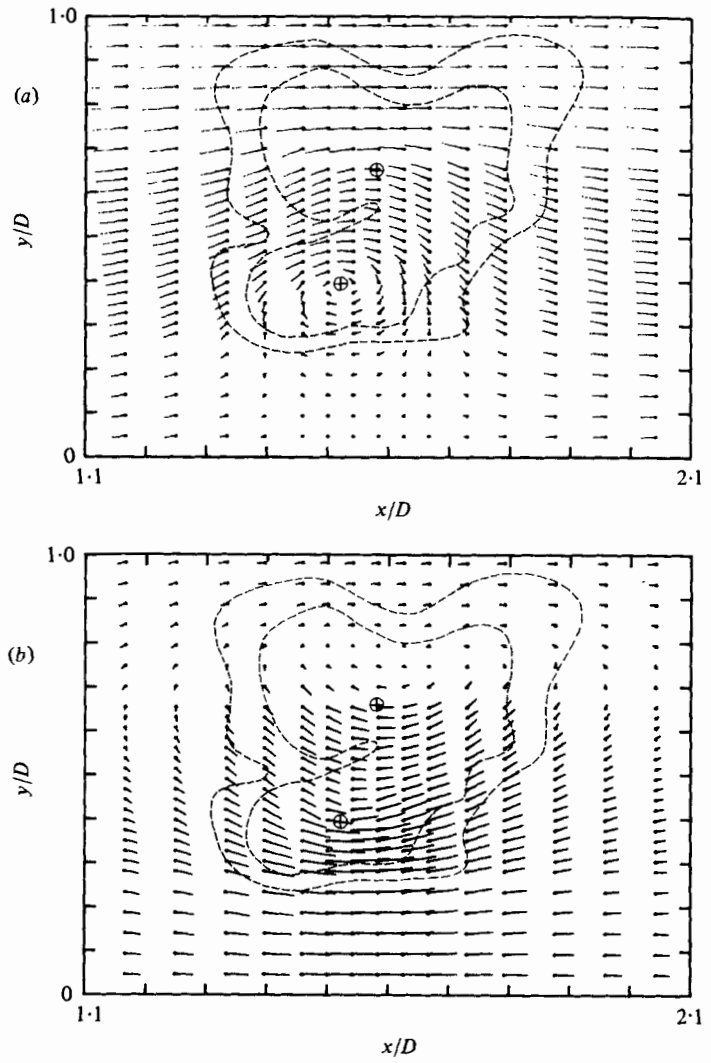

FIGURE 23 (*a*, *b*). For legend see facing page.

is an exact differential. In the present case of unsteady flows, the exact differential of $\langle\psi\rangle(x, r, t)$ is

$$d\langle\psi\rangle = -r\langle v\rangle\,dx + r\langle u\rangle\,dr + \frac{\partial\langle\psi\rangle}{\partial t}\,dt. \tag{3.4b}$$

Note that the continuity equation (3.2) is not only necessary but also sufficient for the existence of the stream function $\langle\psi\rangle$ in a simply connected region (Rektorys 1969). The consequence of $d\langle\psi\rangle$ being an exact differential is that its integral between points (x_1, y_1, t_1) and (x_2, y_2, t_2) is independent of the integration path, i.e.

$$\int_1^2 d\langle\psi\rangle = \langle\psi\rangle_2 - \langle\psi\rangle_1.$$

Note that the azimuthal component $\langle w\rangle$, even if present, is irrelevant to $\langle\psi\rangle$, nor can $\langle\psi\rangle$ be used to deduce $\langle w\rangle$.

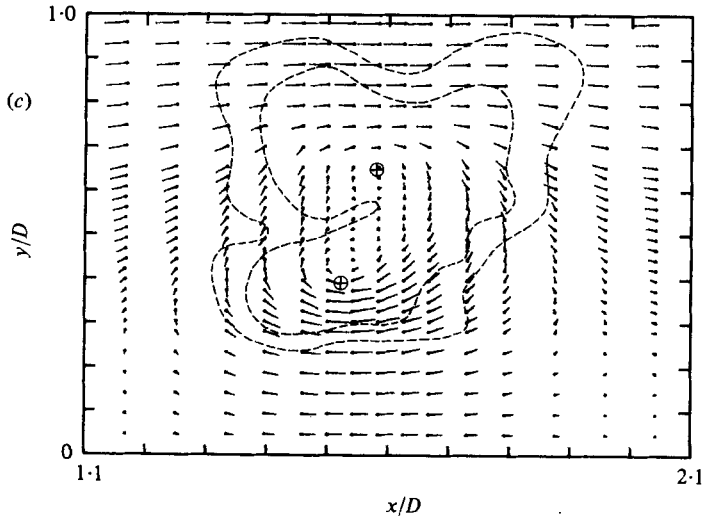

FIGURE 23. Distribution of the velocity vectors in region II with a reference frame velocity of: (*a*) $1{\cdot}25U_e$ (convection velocity of vortex 1); (*b*) $0{\cdot}35U_e$ (convection velocity of vortex 2); (*c*) $0{\cdot}80U_e$.

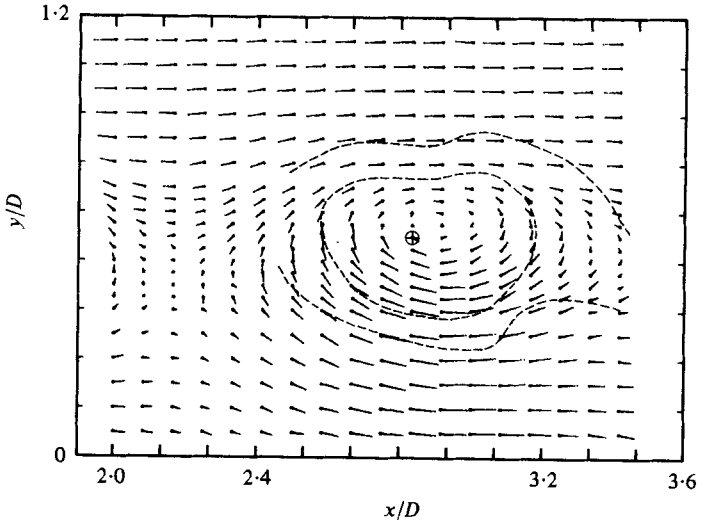

FIGURE 24. Distribution of the velocity vectors in region III with $U_{\text{ref}} = 0{\cdot}54U_e$.

If time is held fixed (i.e. considering a particular phase only) and if integration is carried out in y at a fixed x, then $\langle\psi\rangle$ depends only on y so that at each x

$$\langle\psi\rangle(y;x) = \int_0^y r\langle u\rangle\,dr + \langle\psi_0\rangle. \tag{3.5}$$

Repeating this integration at different x, a spatial distribution of the stream function can be obtained at the selected phase. On the axis of symmetry, it is justifiable to take $\langle\psi\rangle$ to be zero; i.e. $\langle\psi_0\rangle = 0$. Thus, the non-dimensional phase-average stream function $\langle\psi\rangle$ were computed as

$$\langle\psi\rangle(y;x) = \frac{1}{DU_e}\int_0^y r[\langle u\rangle(y;x) - U_{\text{ref}}]\,dr. \tag{3.6}$$

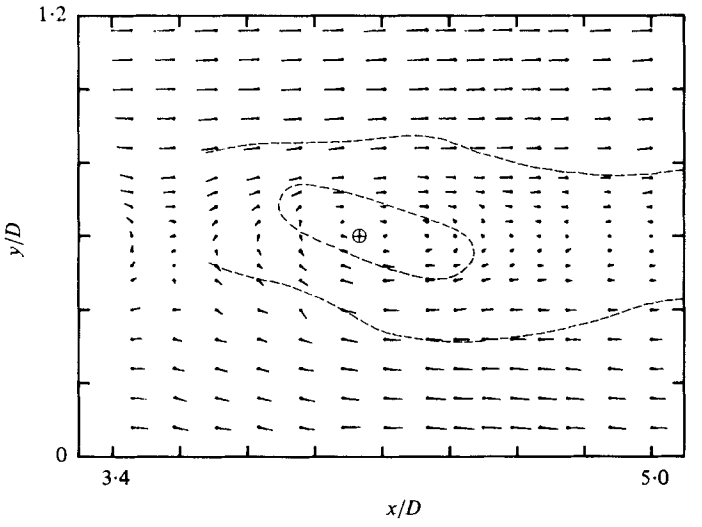

FIGURE 25. Distribution of the velocity vectors in region IV with $U_{ref} = 0{\cdot}58U_e$.

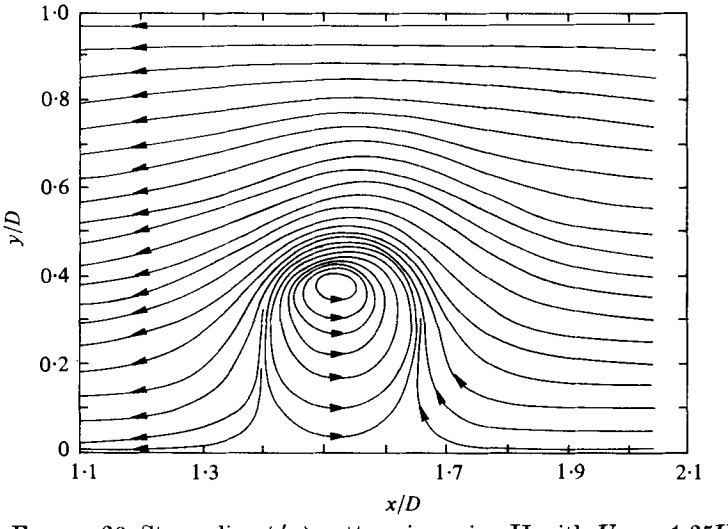

FIGURE 26. Streamline (ψ_p) pattern in region II with $U_{ref} = 1{\cdot}25U_e$.

Since the stream function is not invariant under Galilean transformation, the computed function will depend on the reference frame velocity U_{ref}. Note that these computations do not use the Taylor hypothesis. Because of the assumption of axisymmetry and time independence of $\langle\psi_0\rangle$, the computed functions $\langle\psi\rangle$ are termed *pseudo stream functions*.

The contours of constant values of the phase-average stream function $\langle\psi\rangle$ corresponding to the situations in figures 22–25 are shown in figures 27–30, respectively: figure 27 for region I with $U_{ref} = 0{\cdot}4U_e$; figures 28(*a*), (*b*) and (*c*) for region II with $U_{ref} = 1{\cdot}25$, 0·35 and $0{\cdot}8U_e$, respectively; figure 29 for region III, with $U_{ref} = 0{\cdot}54U_e$; and figure 30 for region IV with $U_{ref} = 0{\cdot}58U_e$. The negative values of $\langle\psi\rangle$ are separated from positive $\langle\psi\rangle$ values by a dotted line for $\langle\psi\rangle = -0{\cdot}01$. Except for the low-speed

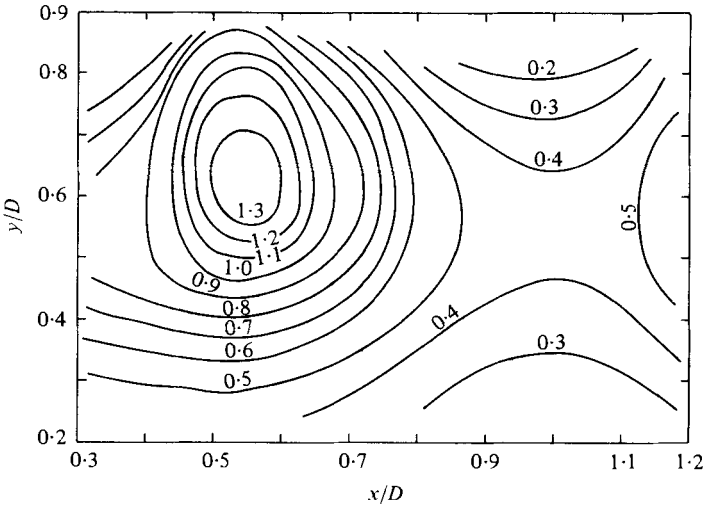

FIGURE 27. Contours of $\langle\psi\rangle$ in region I with $U_{ref} = 0{\cdot}4U_e$.

side, the agreement between the $\langle\psi\rangle$ functions and ψ_p are impressive. Note the close agreement on the locations of 'saddle points' in regions I, III and IV. The low-speed side disagreement between $\langle\psi\rangle$ and ψ_p is not pronounced in region IV (see figures 25 and 30); but, in regions closer to the jet exit, significant differences can be noticed. While the velocity vectors indicate parallel streamlines on the low-speed side, the pseudo-stream-function contours indicate an outward bulge. This difference is most pronounced for region I (compare figures 22 and 27) and is progressively less so farther downstream.

Referring back to figure 16, the dotted portion of the $\langle u\rangle$ profile in (*b*) from point *C* outward is in error owing to the effect of flow reversal and would cause the computed values of $\langle\psi\rangle$ (dotted line in figure 16*d*) to be higher than the actual values (solid line), and thus a constant $\langle\psi\rangle$ line around point *B* (figure 16*a*) would be shifted away from the jet centre-line. Note that this error is cumulative in the computation of $\langle\psi\rangle$. Thus, flow reversal should partly explain the differences on the low-speed side between constant $\langle\psi\rangle$ lines and streamlines ψ_p. However, the reasonable agreement everywhere between $\langle\psi\rangle$ and ψ_p suggests that the assumption of the axisymmetry of the phase-average flow field is reasonable and that single-wire data may be adequate for qualitative description of the coherent structure motion (Zilberman *et al.* 1977; Cantwell *et al.* 1978; Hussain, Kleis & Sokolov 1980).

3.7. *The superimposed random-fluctuation field*

Contours of the phase-average background turbulence intensities $\langle u_r^2\rangle^{\frac{1}{2}}$ and $\langle v_r^2\rangle^{\frac{1}{2}}$ are plotted in figures 31 and 32, respectively, covering the entire flow domain investigated, i.e. for regions I–IV combined. Note that the ordinate is expanded (about 3·7 times) compared to the abscissa scale. In order to capture the details of the flow physics during pairing, the contours of $\langle u_r^2\rangle^{\frac{1}{2}}$ and $\langle v_r^2\rangle^{\frac{1}{2}}$ for the phases 1–4 of the pairing process are shown in figures 33 and 34, respectively. The plus signs approximately locate the vortex centres in figures 31–34. The intensity contours show essentially no difference between

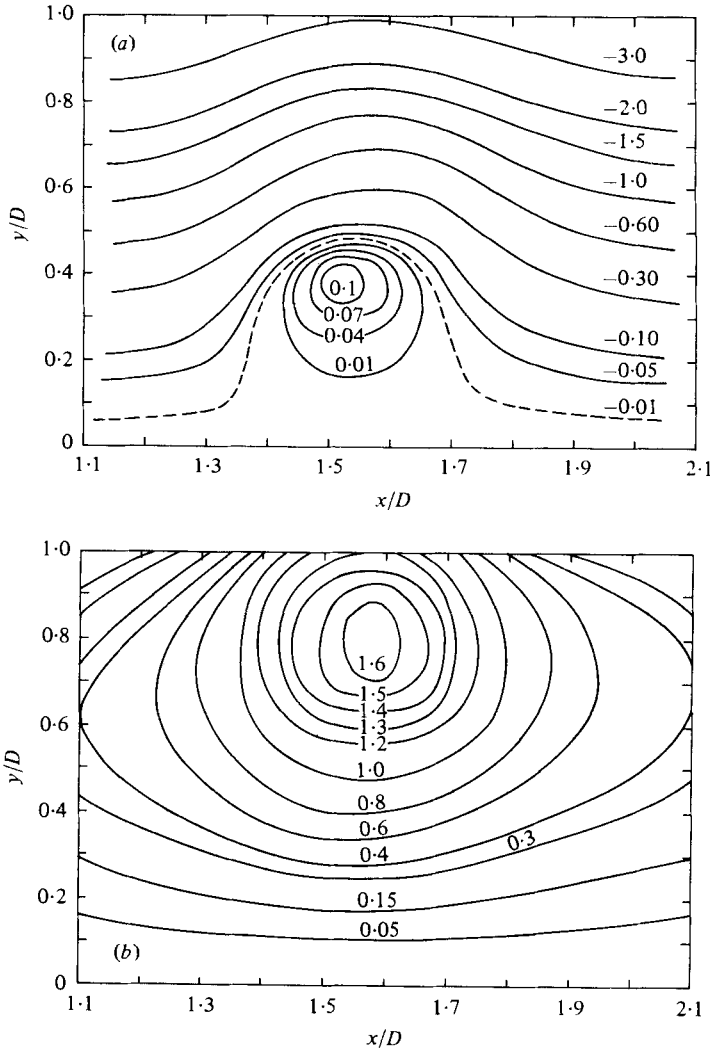

FIGURE 28 (*a*, *b*). For legend see facing page.

$\langle u_r^2\rangle^{\frac{1}{2}}$ and $\langle v_r^2\rangle^{\frac{1}{2}}$, the peak values occur approximately at the vortex centres. In each region the x-extent of any contour is lower for $\langle v_r^2\rangle^{\frac{1}{2}}$ than for $\langle u_r^2\rangle^{\frac{1}{2}}$.

The question naturally arises as to how much of the $\langle u_r^2\rangle^{\frac{1}{2}}$ and $\langle v_r^2\rangle^{\frac{1}{2}}$ data are due to the jitter. In a horizontal line through a vortex centre, $\langle u_p\rangle$ should be zero and on a vertical line, $\langle u_p\rangle$ will have a maximum jump. Conversely for $\langle v_p\rangle$. Consequently, one could argue that slight jitter in the vortex arrival time would contribute to the measured $\langle u_r^2\rangle^{\frac{1}{2}}$, $\langle v_r^2\rangle^{\frac{1}{2}}$ data. At locations where the vortices are small, say in region I, the relative effect can be large. However, in region IV where the coherent structure cross-section is large and the spatial gradients in $\langle u_p\rangle$ and $\langle v_p\rangle$ are small, the peak intensities are still large. Thus at least in regions III and IV where the vortices are turbulent, most of the measured intensities are due to random turbulent fluctuations. It will be apparent from the $\langle u_r v_r\rangle$ contours, that the jitter effect in $\langle u_r^2\rangle^{\frac{1}{2}}$ and $\langle v_r^2\rangle^{\frac{1}{2}}$ contours is not dominant.

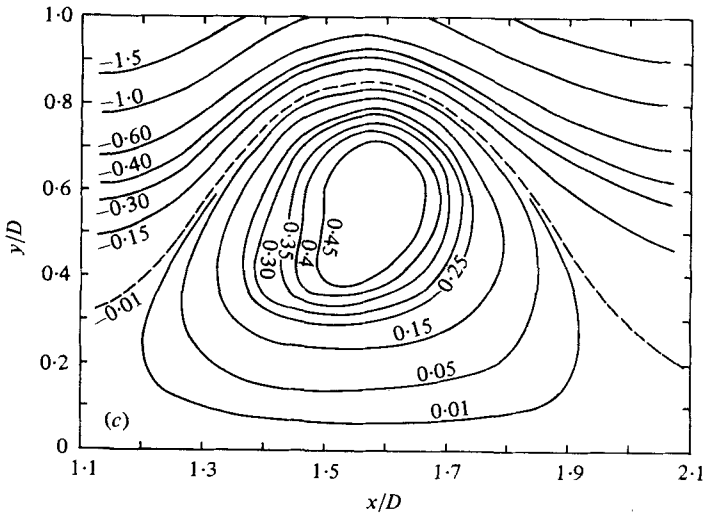

FIGURE 28. Contours of $\langle\psi\rangle$ in region II with: (*a*) $U_{\text{ref}} = 1{\cdot}25U_e$; (*b*) $U_{\text{ref}} = 0{\cdot}35U_e$; (*c*) $U_{\text{ref}} = 0{\cdot}8U_e$.

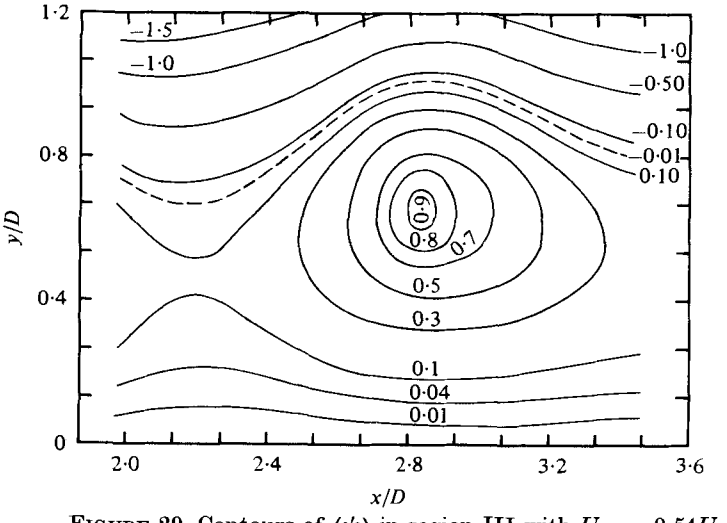

FIGURE 29. Contours of $\langle\psi\rangle$ in region III with $U_{\text{ref}} = 0{\cdot}54U_e$.

In the regions I–IV, the peak values of $|\langle v\rangle|/U_e$ are 0·35, 0·35, 0·25 and 0·10, respectively, while the corresponding $\langle v_r^2\rangle^{\frac{1}{2}}/U_e$ are 0·22, 0·26, 0·20 and 0·15. The corresponding values of $|\langle u_p\rangle|/U_e$ peaks in the four regions are 0·45, 0·55, 0·25 and 0·15, while the values of $\langle u_r^2\rangle^{\frac{1}{2}}/U_e$ peaks are 0·15, 0·18, 0·21 and 0·20, respectively. Thus in regions closer to the exit, the coherent motion velocity oscillations are stronger than those due to background turbulence while, in region IV, the latter becomes stronger than the former. Similar is the case for the Reynolds stress (see later). Closer to the jet exit, $\langle v_r^2\rangle^{\frac{1}{2}}$ peaks are higher than $\langle u_r^2\rangle^{\frac{1}{2}}$ peaks; $\langle u_r^2\rangle^{\frac{1}{2}}$ values generally increase with increasing downstream distance. Cantwell & Coles (1978, private communication) also found $\langle v_r^2\rangle^{\frac{1}{2}}$ higher than $\langle u_r^2\rangle^{\frac{1}{2}}$ peaks in the central regions of the vortices shed from a

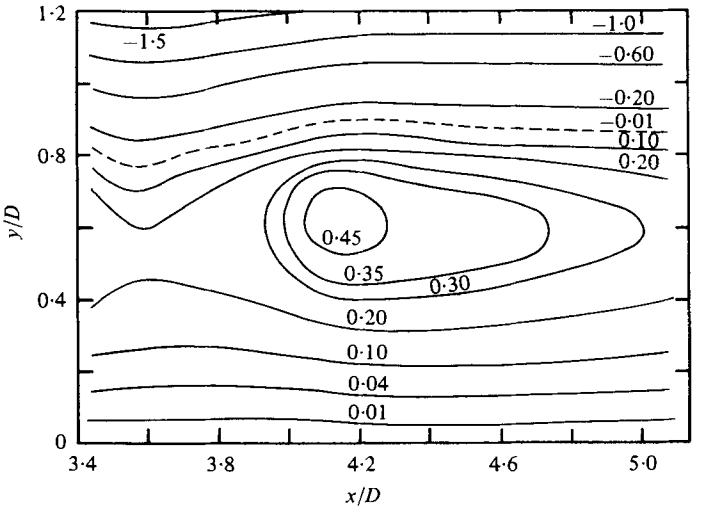

FIGURE 30. Contours of $\langle\psi\rangle$ in region IV with $U_{ref} = 0{\cdot}58U_e$.

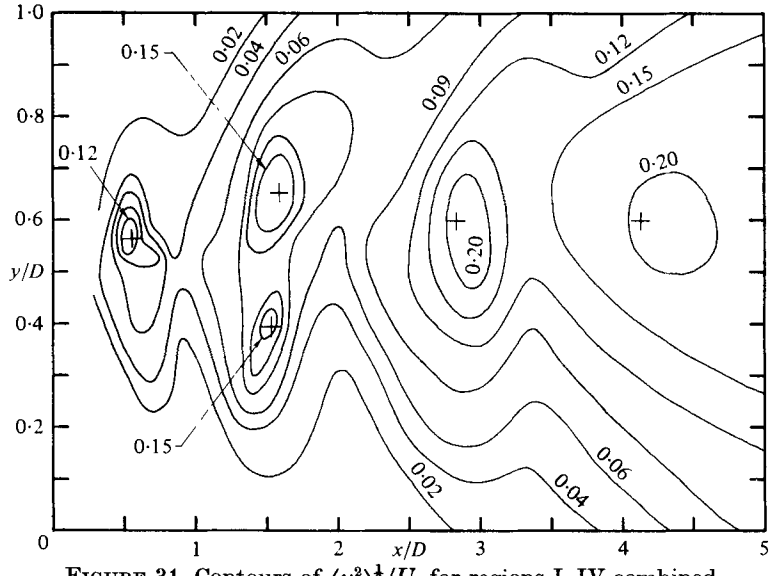

FIGURE 31. Contours of $\langle u_r^2\rangle^{\frac{1}{2}}/U_e$ for regions I–IV combined.

cylinder. As discussed in connexion with figure 19, the larger $\langle v_r^2\rangle^{\frac{1}{2}}$ peaks in their measurements were probably also contributed partly by the phase jitter.

Comparison of the phase-average intensity contours (e.g. $\langle u_r^2\rangle^{\frac{1}{2}}$ in figure 31) with the corresponding time-average contours (e.g. u' in figure 28*a* of I), shows that $\langle u_r^2\rangle^{\frac{1}{2}}$ in general is less than u' everywhere in the flow field. However, phase-average intensities do exceed time-average intensities at some spatial locations by as much as 10 %, especially around the locations of the centres of the vortices. This is not unexpected; a burst of large-amplitude random fluctuations over a short duration (compared to the period) may not affect the total time-average r.m.s. intensity significantly, although phase average r.m.s. intensity measured at that particular phase would be larger.

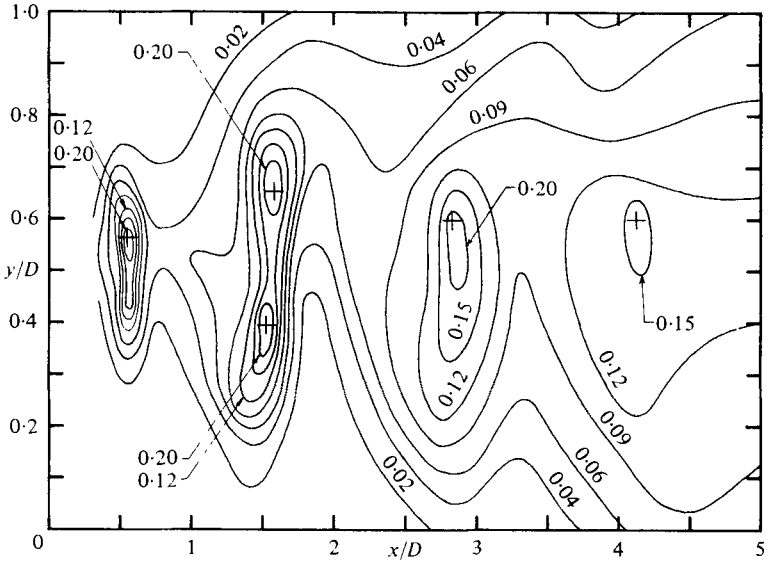

FIGURE 32. Contours of $\langle v_r^2 \rangle^{\frac{1}{2}}/U_e$ for the regions I–IV combined.

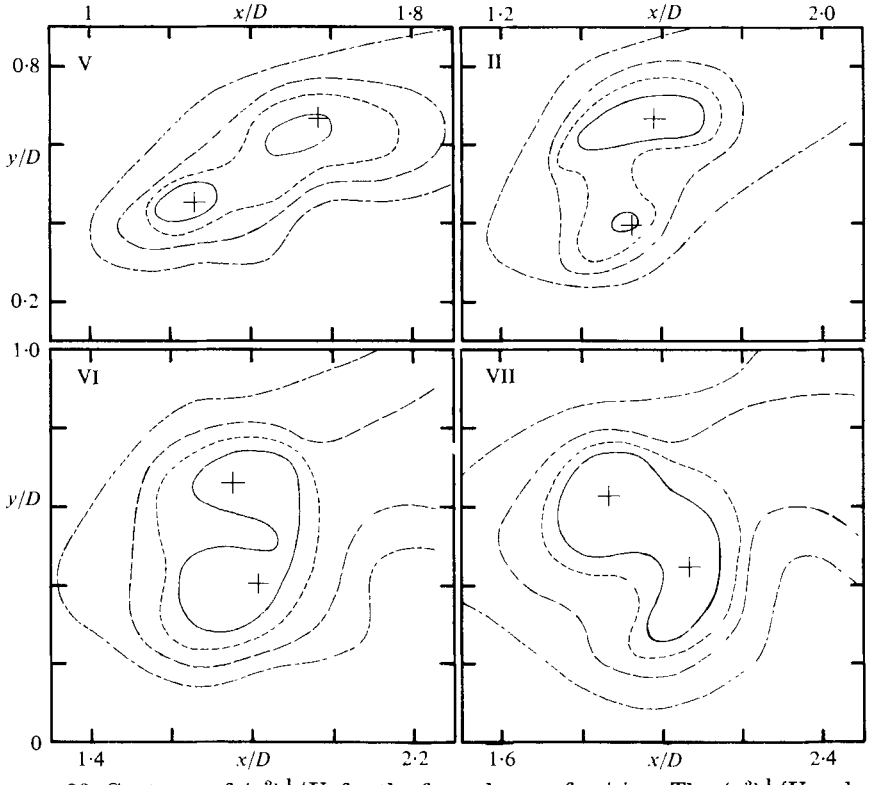

FIGURE 33. Contours of $\langle u_r^2 \rangle^{\frac{1}{2}}/U_e$ for the four phases of pairing. The $\langle u_r^2 \rangle^{\frac{1}{2}}/U_e$ values are: ——, 0·15; – – –, 0·12; — —, 0·09; — — —, 0·06.

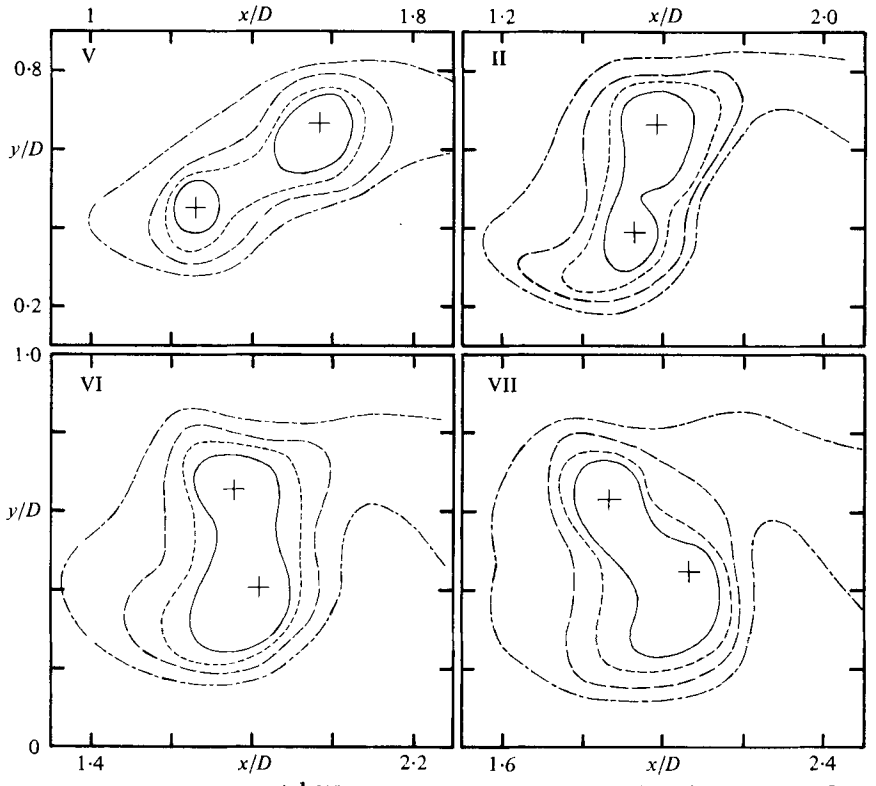

FIGURE 34. Contours of $\langle v_r^2 \rangle^{\frac{1}{2}}/U_e$ for the four phases of pairing. Same line codes are used as in figure 33.

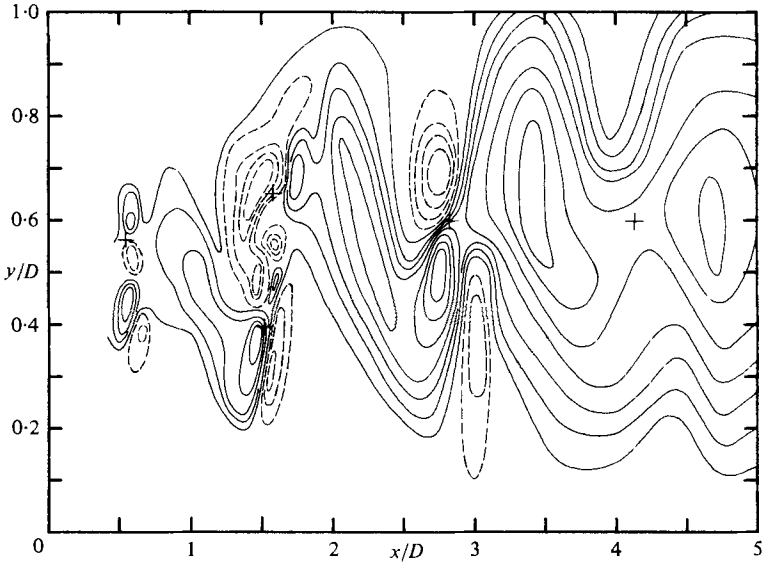

FIGURE 35. Contours of $\langle u_r v_r \rangle/U_e^2$ for regions I–IV combined. Contour values in sequence are: −0·001, −0·002, −0·003, −0·004, −0·006, −0·008, −0·01 (dashed); 0·001, 0·002, 0·003, 0·004, 0·006, 0·008, 0·01 (solid).

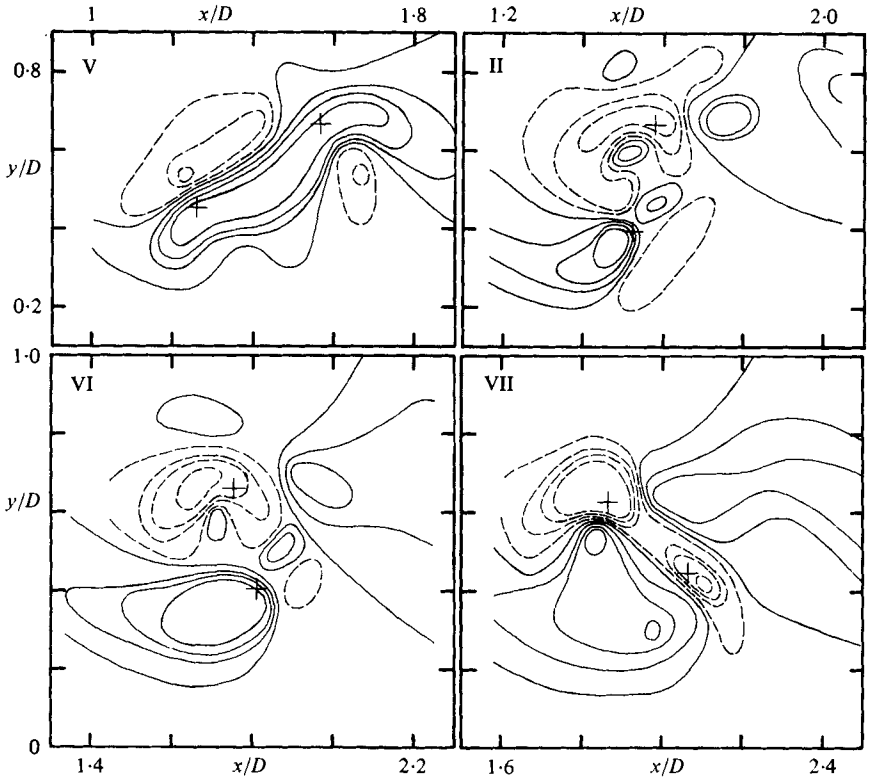

FIGURE 36. Contours of $\langle u_r v_r \rangle / U_e^2$ for the four phases of pairing. Contour values in sequence are: $-0{\cdot}001$, $-0{\cdot}004$, $-0{\cdot}006$, -0.008 (dashed); $0{\cdot}001$, $0{\cdot}004$, $0{\cdot}006$, $0{\cdot}008$ (solid).

Figures 33 and 34, which show the phase-average r.m.s. intensities at the four phases of pairing, confirm the visual observation that vortex 1 in passing from phase 2–3 during pairing, begins its transition to turbulence (see I). The area in the (x, y) plane occupied by a particular contour (e.g. $\langle u_r^2 \rangle^{\frac{1}{2}} / U_e = 0{\cdot}15$) enlarges significantly between phases 2 and 3. This increase and the associated drop in the phase-average vorticity would suggest transition of vortex 1 between phases 2 and 3 of the pairing process.

3.8. *Interaction of background turbulence Reynolds stress with coherent vorticity*

The phase-average distribution of the background turbulence Reynolds stress $\langle u_r v_r \rangle$ is shown in figure 35 for the entire flow region (i.e. regions I–IV combined) at the selected phase. The same co-ordinate scales are used as in figures 31 and 32. Figure 36 shows the $\langle u_r v_r \rangle$ contours of the phases 1–4 of the pairing process. The vortex centres are indicated by the plus sign. Note that the peak $\langle u_r v_r \rangle$ locations do not coincide with those for $\langle u_r^2 \rangle^{\frac{1}{2}}$ and $\langle v_r^2 \rangle^{\frac{1}{2}}$. Note also that the peaks in $\langle u_r v_r \rangle$ are not associated with the regions of steep gradients of $\langle u_p v_p \rangle$ (figure 19). Consequently, the $\langle u_r v_r \rangle$ data as well as the $\langle u_r^2 \rangle^{\frac{1}{2}}$ and $\langle v_r^2 \rangle^{\frac{1}{2}}$ do not contain significant inaccuracies due to phase dispersion or jitter.

The coherent structure organizes the background turbulence such that the phase-average Reynolds stress $\langle u_r v_r \rangle$ acts to destroy the coherent structure vorticity. The

role of the background turbulence on the coherent vorticity can be understood by considering the governing equation for the phase-average vorticity. Using the decomposition (2.1), one can derive the governing equation for the time mean, coherent structure and background turbulent vorticity fields as follows:

$$\frac{\bar{D}}{Dt}\bar{\xi}_i = \bar{\xi}_j\frac{\partial\bar{u}_i}{\partial x_j} + \nu\frac{\partial^2}{\partial x_k\partial x_k}\bar{\xi}_i + \frac{\partial}{\partial x_j}(\overline{\tilde{u}_i\tilde{\xi}_j} - \overline{\tilde{u}_j\tilde{\xi}_i}) + \frac{\partial}{\partial x_j}(\overline{u_i'\zeta_j'} - \overline{u_j'\zeta_i'}); \tag{3.7a}$$

$$\frac{\bar{D}}{Dt}\tilde{\xi}_i = \tilde{\xi}_j\frac{\partial\bar{u}_i}{\partial x_j} + \bar{\xi}_j\frac{\partial\tilde{u}_i}{\partial x_j} + \nu\frac{\partial^2}{\partial x_k\partial x_k}\tilde{\xi}_i + \frac{\partial}{\partial x_j}(\tilde{u}_i\tilde{\xi}_j - \overline{\tilde{u}_i\tilde{\xi}_j}) - \frac{\partial}{\partial x_j}(\tilde{u}_j\tilde{\xi}_i - \overline{\tilde{u}_j\tilde{\xi}_i})$$
$$- \frac{\partial}{\partial x_j}(\tilde{u}_j\bar{\xi}_i) + \frac{\partial}{\partial x_j}(\langle u_i'\zeta_j'\rangle - \overline{u_i'\zeta_j'}) - \frac{\partial}{\partial x_j}(\langle u_j'\zeta_i'\rangle - \overline{u_j'\zeta_i'}); \tag{3.7b}$$

$$\frac{\bar{D}}{Dt}\zeta_i' = (\bar{\xi}_j + \tilde{\xi}_j)\frac{\partial u_i'}{\partial x_j} + \zeta_j'\frac{\partial(\bar{u}_i + \tilde{u}_i)}{\partial x_j} + \nu\frac{\partial^2\zeta_i'}{\partial x_k\partial x_k} - u_j'\frac{\partial}{\partial x_j}(\bar{\xi}_i + \tilde{\xi}_i) - \tilde{u}_j\frac{\partial}{\partial x_j}\zeta_i'$$
$$+ \frac{\partial}{\partial x_j}(\zeta_i'u_i' - \langle\zeta_j'u_i'\rangle) - \frac{\partial}{\partial x_j}(u_j'\zeta_i' - \langle u_j'\zeta_i'\rangle). \tag{3.7c}$$

These equations can be further simplified.

It should be recognized that the coherent structure is not really a perturbation superimposed on the time-mean flow. When the structure is present, the motion is entirely due to the structure. Thus the classical triple decomposition (2.1) should be discarded in favour of a double decomposition, i.e.

$$\zeta_i(\mathbf{x}, t) = \langle\zeta_i\rangle(\mathbf{x}, t) + \zeta_i'(\mathbf{x}, t). \tag{3.8}$$

Phase average of the vorticity equations after this substitution yields

$$\frac{\hat{D}}{Dt}\langle\zeta_i\rangle = \langle\zeta_j\rangle\frac{\partial\langle u_i\rangle}{\partial x_j} + \nu\frac{\partial^2\langle\zeta_i\rangle}{\partial x_k\partial x_k} + \frac{\partial}{\partial x_j}(\langle\zeta_j'u_i'\rangle - \langle u_j'\zeta_i'\rangle). \tag{3.9}$$

The left-hand side represents the rate of change of the phase-average vorticity of a fluid element moving in the phase-average flow field. The first term on the right-hand side represents coherent vorticity augmentation through stretching by the coherent motion; the second term represents the coherent vorticity diffusion and the last term is the destruction or production of coherent vorticity by the background turbulence field.

Simple reasoning can be used to simplify equation (3.9). If R is the characteristic size of the structure, then

$$\langle\zeta_j\rangle\frac{\partial\langle u_i\rangle}{\partial x_j} = O\left(\frac{U_e^2}{R^2}\right), \quad \nu\frac{\partial^2\langle\zeta_i\rangle}{\partial x_k\partial x_k} = O\left(\frac{\nu U_e}{R^3}\right), \quad \frac{\partial\langle u_i'\zeta_j'\rangle}{\partial x_j} = O\left(\frac{v^2}{\lambda R}\right), \tag{3.10}$$

assuming that $\langle u\rangle \sim U_e$; $\langle\zeta\rangle \sim U_e/R$; $u' \sim v$; $\zeta' \sim v/\lambda$ and that u' and ζ' are well correlated; λ is the Taylor microscale, i.e. $\langle(\partial u_i'/\partial x_j)(\partial u_i'/\partial x_j)\rangle = v^2/\lambda^2$. Since $\lambda \ll R$, the ratio of the first to the second terms in (3.10) is the Reynolds number U_eR/ν which is large. That is, the coherent structure dynamics is essentially inviscid. Viewed another way, the ratio of the structure transit time $\tau_t \sim R/U_e$ to the vorticity diffusion time $\tau_d \sim R^2/\nu$, i.e. $\tau_t/\tau_d = \nu/U_eR$ is very small. Thus, viscous diffusion is too slow to be important in the coherent structure dynamics.

The ratio of the first term to the third in (3.10) is $(U_e^2/\nu^2)(\lambda/R)$. However, in the jet and free shear layer $\nu \sim U_e$ while $\lambda \ll R$. Thus, the vortex stretching term is comparatively weaker. (On the basis of physical arguments, the axisymmetric structure will have negligible vortex stretching except during the pairing event when there are noticeable changes in the vortex toroid diameter.) Thus,

$$\frac{\hat{D}}{Dt}\langle\zeta_i\rangle = \frac{\partial}{\partial x_j}(\langle\zeta_j' u_i'\rangle - \langle u_j'\zeta_i'\rangle). \tag{3.11a}$$

Since we are interested in the $\langle\zeta_3\rangle \equiv \Omega$ component only,

$$\frac{\hat{D}\Omega}{Dt} = \frac{\partial}{\partial x_j}(\langle\zeta_j' u_3'\rangle - \langle u_j'\zeta_3'\rangle). \tag{3.11b}$$

It is clear that the correlation between velocity and vorticity fluctuations is the principal contributor to the production or destruction of phase-average vorticity. The coherent structure organizes the background fluctuation field such that the otherwise random vortex forces $\mathbf{u}\times\boldsymbol{\zeta}$ are organized to strengthen/dilute the structure coherent vorticity. For a flow whose phase average field is two-dimensional, it is easy to show that

$$\frac{\partial}{\partial y}\langle u_r v_r\rangle = \langle w_r\zeta_2\rangle - \langle v_r\zeta_3\rangle. \tag{3.12}$$

Neglecting gradients of dynamic pressure, equation (3.11*b*) becomes

$$\frac{\hat{D}\Omega}{Dt} = -\frac{\partial^2}{\partial x^2}\langle u_r v_r\rangle + \frac{\partial^2}{\partial y^2}\langle u_r v_r\rangle. \tag{3.13}$$

Thus at any point where the phase average of the background Reynolds stress $\langle u_r v_r\rangle$ has a minimum in x and maximum in the radial direction, there will be maximum decrease of phase-average vorticity. That is, at the *saddle points* in the $\langle u_r v_r\rangle$ contours, the effect of the background turbulence on the destruction of the coherent vorticity will be the maximum. Figure 35 shows that the peaks of phase-average vorticity are located near the saddle points of the $\langle u_r v_r\rangle$ contours, especially in regions III and IV.

The right-hand side of (3.13) estimated through graphical differentiation of $\langle u_r v_r\rangle(x)$ and $\langle u_r v_r\rangle(y)$ through the saddle point accounts for the observed peak vorticity drop from region III to IV. Figure 12 shows that this drop $\delta\Omega$ is about $-2{\cdot}0 f_p$ ($= 140\,\mathrm{s}^{-1}$). Since the time elaspsed δt between these two regions is 29 ms,

$$\hat{D}\Omega/Dt \approx \delta\Omega/\delta t \simeq 4800\,\mathrm{s}^{-2}.$$

The estimated value of the right-hand side of (3.13), taken as an average of the values determined from graphical differentiation at these two regions, is $-4500\,\mathrm{s}^{-2}$. This amazing agreement should not be taken too seriously because of the large uncertainty in the computation of the second derivatives, but is a reasonable confirmation of the role of $\langle u_r v_r\rangle$ via (3.13).

3.9. *Circumferential correlations*

In an attempt to understand further the transition process, circumferential correlation (both time-mean and phase-locked) measurements were made with two single-wire

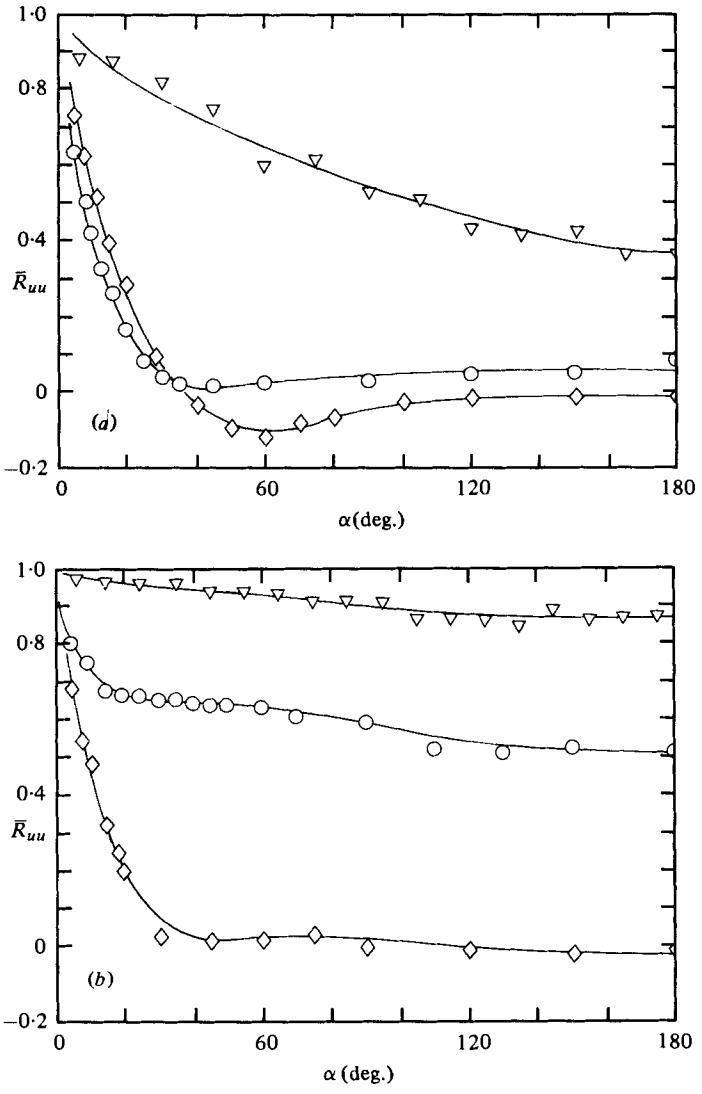

FIGURE 37. Time-mean circumferential correlation $\bar{R}_{uu}$ *vs.* α; $Re_D = 32000$, 7·62 cm jet; ▽, $x/D = 1{\cdot}5$ ($y/D = 0{\cdot}33$); ○, $x/D = 2{\cdot}8$ ($y/D = 0{\cdot}40$); ◇, $x/D = 4.13$ ($y/D = 0{\cdot}47$). (*a*) Unexcited; (*b*) excited at $St_D = 0{\cdot}85$.

probes: probe 1 was held at a certain radius r, while probe 2 was moved azimuthally (in α) keeping its orientation and radial displacement r the same in a plane perpendicular to the jet axis. The azimuthal traverse of the second probe was facilitated by a probe holder with an arm of variable radial displacement, the holder being rotated about an axis aligned with the jet axis. Alignment of the axes was done by trial until constant readings of U at any α were obtained. Measurements were made at three x stations, $x/D = 1{\cdot}5$, 2·8 and 4·13, at the radial locations $y/D = 0{\cdot}33$, 0·40 and 0·467, respectively. The choice of these three radii was based on the core size of the vortices at these locations, so that the ratio of the vorticity encountered by the probe at the phase of the measurement and the core peak vorticity was approximately the same at each

location (see figures 11*b*, *c*, *d*). Values of U/U_e at these three locations were about 0·9, 0·8 and 0·6, respectively.

Figure 37(*a*) shows the conventional, two-point streamwise velocity correlation coefficient $\bar{R}_{uu}$ (i.e. $R_{11}(0, 0, \alpha)$) as a function of angular separation α for the unexcited jet at $Re_D = 32000$. At $x/D = 1{\cdot}5$, the correlation drops gradually with α and at $\alpha = 180°$ it is about 0·4. Thus, the randomly occurring structures in an unexcited jet are initially circumferentially well-correlated. The drop-off of $\bar{R}_{uu}$ is much faster at both the later axial stations; at $x/D = 4{\cdot}13$, the circumferential correlation is lost at about $\alpha = 35°$. These correlation results at $x/D = 2{\cdot}8$ and 4·13 agree qualitatively with those of Bradshaw, Ferriss & Johnson (1964). The higher values of $\bar{R}_{uu}$ at $x/D = 4{\cdot}13$ (for $\alpha \lesssim 35°$) than those at $x/D = 2{\cdot}8$ can be traced to the dependence of $\bar{R}_{uu}$ on r (radius). For a fixed x and a fixed α, $\bar{R}_{uu}$ is found to be a function of r, $\bar{R}_{uu}$ being least in the high shear regions. Measurements by Lau (1978, private communication) show similar dependence of $\bar{R}_{uu}$ on r.

The time-mean circumferential correlation increases remarkably when the jet is excited at $St_D = 0{\cdot}85$ to induce stable vortex pairing in the jet-column mode (figure 37*b*). At $x/D = 1{\cdot}5$, almost perfect correlation is observed all around the circumference. This strong axisymmetry indicates that the slight jitter in the passage of vortex 1 observed at $x/D = 1{\cdot}5$ (§ 3.3), is probably in its arrival time rather than due to 'wobbly' motions associated with the circumferential lobe structure. Substantial circumferential correlation $\bar{R}_{uu}$ is still maintained at $x/D = 2{\cdot}8$, where the paired vortex is found to have already undergone transition. Notice for this location that about 35 % drop in $\bar{R}_{uu}$ occurs within only about 20° while, for the rest of α range, $\bar{R}_{uu}$ is essentially constant. The fast drop of $\bar{R}_{uu}$ within a short angular distance can be ascribed to the small-scale random fluctuations superimposed on the nearly axisymmetric coherent structure, the latter producing the flat $\bar{R}_{uu}$ variation for the rest of the circumference. Thus, the $\bar{R}_{uu}$ data are consistent with the inference made that the vortices undergo transition near the end of the pairing event. The $\bar{R}_{uu}(\alpha)$ variation at $x/D = 4{\cdot}13$, for $St_D = 0{\cdot}85$ is comparable to that for $St_D = 0$, indicating significant weakening of the coherent structure by the end of the potential core, even though better organized initially by the controlled excitation.

In order to obtain information on the instantaneous vortical structure, it is necessary to measure phase-locked circumferential correlation at specific configurations of the coherent structures. This correlation coefficient is defined as follows:

$$\langle R_{u_1 u_2} \rangle(\alpha) = \frac{\langle u_1(0)\, u_2(\alpha) \rangle}{\langle u_1^2(0) \rangle^{\frac{1}{2}} \langle u_2^2(\alpha) \rangle^{\frac{1}{2}}}, \tag{3.14}$$

where u_1 and u_2 are departures from the local time-mean axial velocities. A third probe was used at $x/D = 1{\cdot}5$, $r/D = 0$ in order to obtain the triggering signal (§ 2.2*a*). Variation of $\langle R_{uu} \rangle$ together with measured U and $\langle u \rangle$ as functions of the phase delay ϕ are shown in figure 38 for fixed angular separation of $\alpha = 90°$. Notice the strong periodic variation of $\langle u \rangle$ caused by the periodic passage of the vortices. For a fixed α, $\langle R_{uu} \rangle$ clearly shows strong dependence on the phase ϕ. Such behaviour should be expected. For example, around the phases where $\langle u \rangle(\phi)$ and U intersect each other (i.e. at $\phi \approx 90°$ and 270°), the product term $u(\alpha = 0°)\, u(\alpha = 90°)$ would be nearly equal to zero since u is zero at all α, while this term will be the maximum at phases $\phi \simeq 0$ and

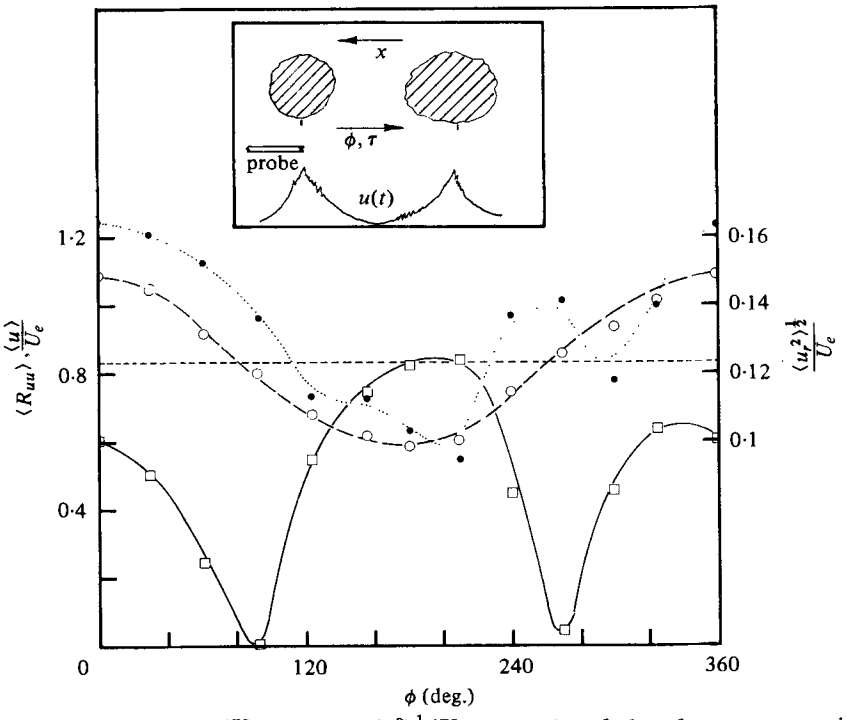

FIGURE 38. Variations of $\langle u\rangle/U_e$ (—○—), $\langle u_r^2\rangle^{\frac{1}{2}}/U_e$ (...●...) and the phase-average circumferential correlation $\langle R_{uu}\rangle$ (—□—) with the phase ϕ; $x/D \approx 2{\cdot}8$, $y/D \approx 0{\cdot}47$, $\alpha \approx 90°$.

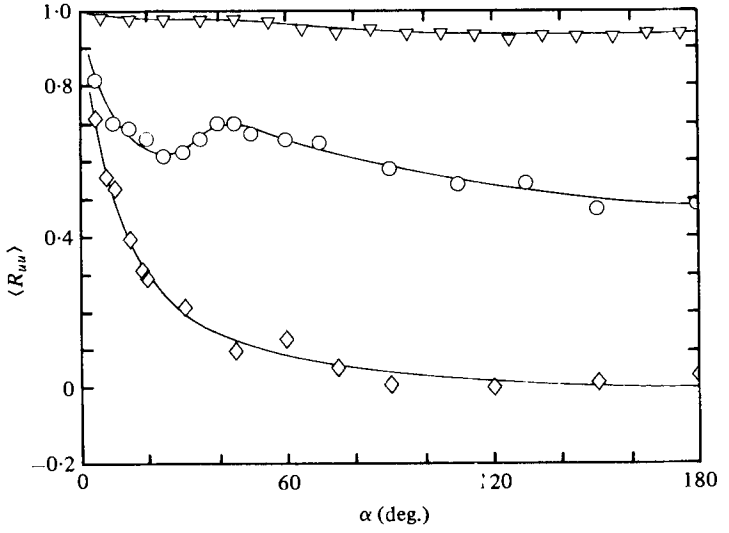

FIGURE 39. $\langle R_{uu}\rangle$ *vs.* α for the phase $\phi = 0$ in figure 38. Symbols represent the same flow conditions as in figure 37.

180°. The probe location with respect to the vortices and the corresponding time trace of the hot-wire signal is shown schematically in the inset in figure 38. The difference between $\langle R_{uu} \rangle$ values at $\phi \simeq 0$ and $\phi \simeq 180°$ is due to the fact that the radial position of the measurement hot wire was such that at $\phi = 0°$ or 360° it is inside the vortex core which is turbulent at this x location, while at $\phi \simeq 180°$ it is in the potential flow between the two vortical structures.

The circumferential correlation $\langle R_{uu} \rangle$, at the phase $\phi = 0$ corresponding to the data in figure 38, are shown in figure 39 for $x/D = 1{\cdot}5$, 2·8 and 4·13. The radial locations at each x are the same as in figures 37 (*a*) and (*b*). Note that this particular phase corresponds to the radial configuration of the two pairing vortices at $x/D = 1{\cdot}5$ and thus show the circumferential correlations on the inner side of vortex 1 in region II as well as those on the inner sides of the paired vortices in regions III and IV (see figures 11 *b*, *c*, *d*). Figure 39 clearly shows that vortex 1, which has been squeezed inside vortex 2 at $x/D = 1{\cdot}5$, still maintains almost perfect circumferential correlation. For region IV (i.e. at $x/D \simeq 4{\cdot}13$), the rapid drop of $\langle R_{uu} \rangle$ with α suggests almost complete breakdown of the well-defined ring structure found at earlier x stations. Note that the decrease of $\langle R_{uu} \rangle$ with α is slightly less than that of $\bar{R}_{uu}$ (figure 37 *b*).

The variation of $\langle R_{uu} \rangle (\alpha)$ at $x/D = 2{\cdot}8$ shows a distinct hump at around $\alpha \simeq 40°$ confirmed by repeated measurements. This hump can probably be explained by an organized three-dimensional structure on the inner periphery of the paired vortex at this location. Smoke visualization experiments indicated that the paired vortex at this location is transitional, resulting in rapid diffusion of the smoke traces, and being associated with azimuthal jet-like ejections radiating outwards in this general area. It is possible that, like the circumferential lobe structure that develop in impulsively created vortex rings (Widnall 1975; Saffman 1978), the attainment of three-dimensionality by the vortices here occurs through some organized core instability of the ring vortices. In a circular jet, the transition of the ring vortices through circumferential instability 'waves' has been observed visually among others by Yule (1978), Davies & Baxter (1978) and Browand & Laufer (1975). Yule observed evolution of the lobe structure essentially at the same x/D location as found here, i.e. $x/D \simeq 3$. It appears from the present data that the breakdown of the paired vortex is also associated with the development of such azimuthal lobe structures. The number of organized azimuthal lobes, since the hump occurs at about 40°, would be about 9.

The question naturally arises as to why only one hump appears instead of 4–5 humps over the α span of 180°. This is easily reconciled by the fact that a circumferential lobe structure associated with the vortex transition cannot be expected to be exactly repeatable from vortex to vortex. The spatial and temporal dispersions in the lobe structure as well as the jitter in the vortex arrival time together with the superimposed turbulence would act to damp out the peaks in $\langle R_{uu} \rangle (\alpha)$ at large α. Thus, the second hump is quite likely too small to be distinguished from the data scatter. Note that any azimuthal rotation of the vortices (Widnall 1975) and jitter in the number of lobes would also affect these measurements. In fact, in order to get repeatable data, the number of realizations used in obtaining $\langle R_{uu} \rangle$ had to be as high as 4000 at each α. The uncertainty in the $\langle R_{uu} \rangle$ data was found to be 5 % on the basis of repeated tests while keeping the measurement probes at fixed locations.

4. Concluding remarks

Coherent ring-like vortical structures could be educed as far downstream as the end of the potential core. The paired vortex structure, however, becomes weaker with increasing downstream distances and no attempt was made in this study to educe the structure farther downstream. It is believed that by elimination of the jitters in the sampled data by alignment through cross-correlation (Sokolov *et al.* 1980; Hussain *et al.* 1980) or some other conditional data acquisition, the coherent structures can be traced farther downstream. How far these structures can be tracked is presently an open question; this is being studied by our group.

During the pairing process, shortly after passing through the radial configuration, the faster-moving inner vortex undergoes an explosive transition to turbulence before losing its identity through merger with the outer vortex. This observation was first made from flow visualization and is supported by the loss of time-mean circumferential correlation $\bar{R}_{uu}(\alpha)$ between regions II and III, by the rapid decrease of the peak vorticity of the inner vortex as it passes through the radial configuration, and by the significant spread of the phase-average turbulence intensity contours from phase 2 to phase 3 of the pairing event. Controlled excitation, though successful in organizing the initial roll-up of the coherent structure near the jet exit, and retaining azimuthal coherence even after transition following the pairing event, appears ineffective in retaining the organization at the end of the potential core. Phase-average circumferential correlation $\langle R_{uu} \rangle (\alpha)$ suggests that the breakdown of the initially organized coherent structure occurs through large-scale azimuthal lobe structures similar to those found in the instability of a thin laminar vortex ring. The vorticity contours show that the 'braid' between two vortex rings does not contain significant amounts of vorticity. The distortions of the measured vorticity contours or the computed pseudo-stream-functions on the low-speed side have been shown to be due to the phase jitter of the structure and signal rectification by the hot wire during instants of flow reversal.

Up to about $x/D = 3$, the measured correlation $\langle u_p v_p \rangle$ (due to the coherent structure) is found to be much larger than $\langle u_r v_r \rangle$ (due to the background turbulence), indicating that large-scale transport by the vortical structures dominates the flow dynamics. In region IV, i.e. about 4 diameters downstream, values of $\langle u_r v_r \rangle$ and $\langle u_p v_p \rangle$ are found to be comparable, indicating that a major role in transport is played by the superimposed random field. However, the jitter in the arrival times of the paired vortex at this location is believed also to contribute to an apparent reduction in $\langle u_p v_p \rangle$ and a corresponding increase in $\langle u_r v_r \rangle$. The coherent structure organizes the random background turbulence such that the background turbulence Reynolds stress is most effective in modifying the phase coherent vorticity. The regions of peak phase-average vorticity especially following the transition of the vortical structures have been shown to occur in regions of 'saddle points' of $\langle u_r v_r \rangle$. Simple analytical reasoning shows that such saddle points of $\langle u_r v_r \rangle$ should contribute to the destruction of coherent structure vorticity.

The transverse transport of u momentum by the coherent structures, as inferred from a 'zone-average correlation', is found to be much larger during the pairing process than in regions where a single vortex is situated. This observation qualitatively supports the claim of Browand & Wiedman (1976) and also confirms the conclusions drawn earlier from the time-average σ_{uv} data (see I). While Browand & Wiedman computed

'average' correlation coefficients by a fixed probe over the time span extending over the passage of the vortical structures, the present study involves correlations over the spatial extent (in x) of the vortical structures at fixed times (phases) and is thus independent of the Taylor hypothesis. The present study further shows that such 'zone-average correlation' is much lower for single vortical structures, both before and after a pairing stage and that the coherent-structure Reynolds stress resulting from structure interaction is much larger at an earlier rather than a later phase of the pairing process.

Contours of phase-average coherent Reynolds stress show alternate regions of positive and negative values. Thus negative production – which contradicts gradient transport hypotheses and turbulence modelling theories – can be explained by coherent structure motions and their interactions.

For characterizing the coherent structure in a turbulent shear flow it appears that the double decomposition, i.e. $f = \langle f \rangle + f'$ (Hussain 1977) is more meaningful than the triple decomposition (Hussain & Reynolds 1970; Cantwell & Coles 1978, private communication).

To what extent are these detailed data on structures induced by controlled excitation related to the practical situation? It is our contention that the controlled excitation does not create an artificial structure but triggers a naturally occurring one. Thus the coherent-structure evolution recorded here should not be drastically different from that of natural structures, especially when they undergo pairing. (In fact, the streamline pattern, aspect ratio and spacing of the structures following the pairing agree quite well with those of the naturally occurring structures (Yule 1978). Yule also found that no pairing occurred beyond $x/D \simeq 2$.) The controlled excitation enabled us to phase-lock onto the structure and derive its characteristics in such details that are unlikely to be possible with the naturally occurring structures. The eduction of the naturally occurring structures is complicated by not only the large dispersions in shapes, sizes, orientations and interactions but also the large radial variations in the organization of the structures, their trajectories and convection velocities (Lau & Fisher 1975; Bruun 1977; Yule 1978; Lau 1978, private communication).

Apart from understanding the flow physics in the near flow field of a circular jet, another goal of this study was to obtain basic information regarding the quasi-deterministic characteristics of the coherent structures and their interactions with the hope that an appropriate (random) distribution of these structures may produce a realistic model of shear-flow turbulence. Data presented in this paper should be utilized in theoretical efforts in that direction.

We are grateful to the Office of Naval Research and the N.A.S.A. Langley Research Center for financial support, to Professor L. S. G. Kovasznay for a careful review of the manuscript, and to him, Professors S. J. Kleis and F. K. Browand for illuminative discussions on the data.

REFERENCES

BATCHELOR, G. K. 1970 *An Introduction to Fluid Dynamics.* Cambridge University Press.

BRADSHAW, P., FERRISS, D. H. & JOHNSON, R. F. 1964 *J. Fluid Mech.* **19**, 591.

BROWAND, F. K. & LAUFER, J. 1975 *Turb. Liquids, Univ. of Missouri-Rolla*, **5**, 333–344.

BROWAND, F. K. & WIEDMAN, P. D. 1976 *J. Fluid Mech.* **76**, 127.

BROWN, G. L. & ROSHKO, A. 1974 *J. Fluid Mech.* **64**, 775.

BRUUN, H. H. 1977 *J. Fluid Mech.* **64**, 775.

CANTWELL, B., COLES, D. & DIMOTAKIS, P. 1978 *J. Fluid Mech.* **87**, 641.

COLES, D. & BARKER, S. J. 1975 *Turbulent Mixing in Nonreactive and Reactive Flows* (ed. S. N. B. Murthy), p. 285. Plenum.

CORCOS, G. M. & SHERMAN, F. S. 1976 *J. Fluid Mech.* **73**, 241.

CROW, S. C. & CHAMPAGNE, F. H. 1971 *J. Fluid Mech.* **48**, 547.

DAVIES, P. O. A. L. & BAXTER, D. R. J. 1978 *Structure and Mechanisms of Turbulence I* (ed. H. Fielder), Lecture Notes in Physics, vol. 75, p. 125. Springer.

HUSSAIN, A. K. M. F. 1977 *Cardiovascular Flow Dynamics and Measurements* (ed. N. H. C. Hwang and N. Norman), p. 541. University Park Press.

HUSSAIN, A. K. M. F., KLEIS, S. J. & SOKOLOV, M. 1980 *J. Fluid Mech.* **98**, 97.

HUSSAIN, A. K. M. F. & REYNOLDS, W. C. 1970 *J. Fluid Mech.* **41**, 241.

HUSSAIN, A. K. M. F. & THOMPSON, C. A. 1980 *J. Fluid Mech.* **100**, 397.

HUSSAIN, A. K. M. F. & ZAMAN, K. B. M. Q. 1975 *Proc. 3rd Interagency Symp. Transp. Noise, Univ. of Utah*, pp. 314–325.

KOVASZNAY, L. S. G., KIBENS, V. & BLACKWELDER, R. F. 1970 *J. Fluid Mech.* **41**, 283.

LAU, J. C. & FISHER, M. J. 1975 *J. Fluid Mech.* **67**, 299.

LIN, C. C. 1953 *Quart. Appl. Math.* **10**, 295.

REKTORYS, K. 1969 *Surveys of Applicable Mathematics.* Massachusetts Institute of Technology Press.

REYNOLDS, W. C. & HUSSAIN, A. K. M. F. 1972 *J. Fluid Mech.* **54**, 263.

SAFFMAN, P. G. 1978 *J. Fluid Mech.* **84**, 625.

SOKOLOV, M., HUSSAIN, A. K. M. F., KLEIS, S. J. & HUSAIN, Z. D. 1980 *J. Fluid Mech.* **98**, 65.

WINANT, C. D. & BROWAND, F. K. 1974 *J. Fluid Mech.* **63**, 237.

WIDNALL, S. 1975 *Ann. Rev. Fluid Mech.* **7**, 141.

WYGNANSKI, I., SOKOLOV, M. & FRIEDMAN, D. 1976 *J. Fluid Mech.* **78**, 785.

YULE, A. J. 1978 *J. Fluid Mech.* **89**, 413.

ZAMAN, K. B. M. Q. 1978 Ph.D. dissertation, University of Houston.

ZAMAN, K. B. M. Q. & HUSSAIN, A. K. M. F. 1980 *J. Fluid Mech.* **101**, 449.

ZAMAN, K. B. M. Q. & HUSSAIN, A. K. M. F. 1981 *J. Fluid Mech.* (to appear).

ZILBERMAN, M., WYGNANSKI, I. & KAPLAN, R. E. 1977 *Phys. Fluids Suppl.* **20**, S258.

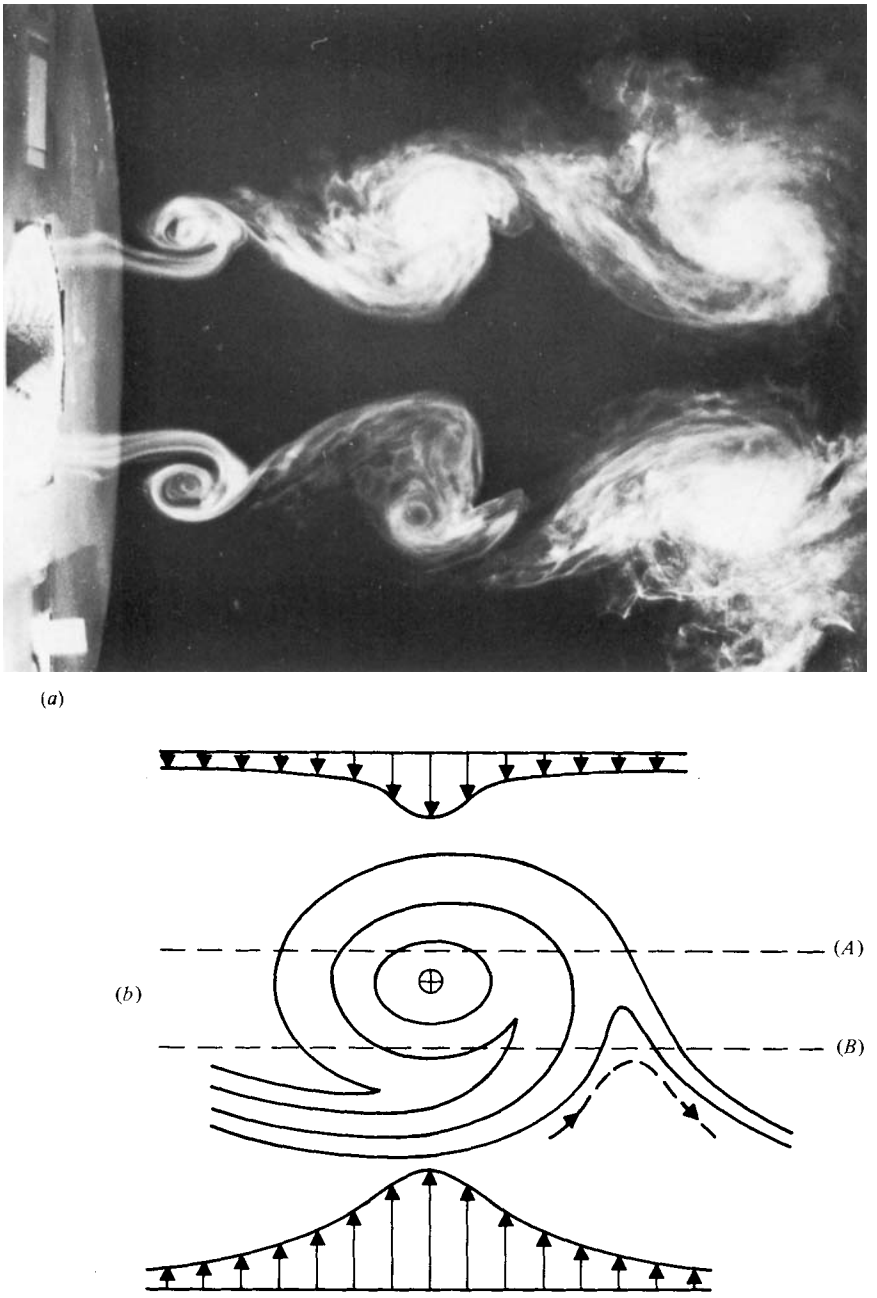

FIGURE 9. (*a*) Smoke-streak picture of the flow. (*b*) Explanation for $\langle u_p \rangle (x)$ induced by the rolled-up vortex in region I.

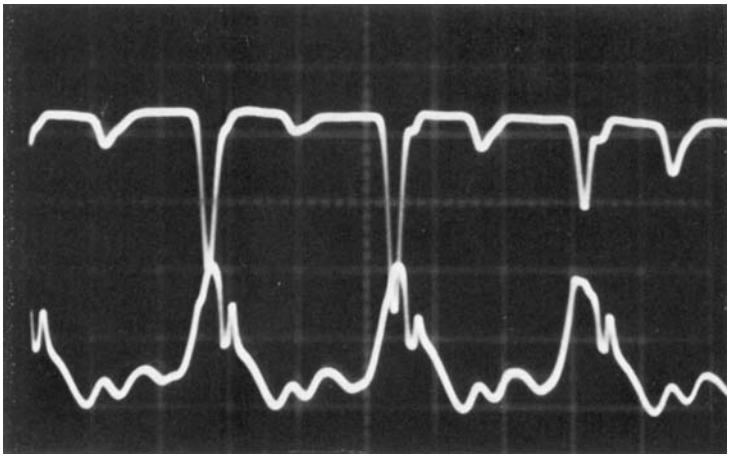

FIGURE 15. Dual-channel oscilloscope traces from a cold-wire–hot-wire pair sensor located at $x/D = 0{\cdot}6$ at the transverse location where $U/U_e \approx 0{\cdot}10$. Upper trace is the temperature signal (inverted), and the lower trace is the u signal.